

The accretion process in the DQ Tau binary system

E. FIORELLINO,¹ S. PARK,¹ Á. KÓSPÁL,^{1,2,3} AND P. ÁBRAHÁM^{1,3}

¹*Konkoly Observatory, Research Centre for Astronomy and Earth Sciences, Eötvös Loránd Research Network (ELKH), Konkoly-Thege Miklós út 15-17, 1121 Budapest, Hungary*

²*Max Planck Institute for Astronomy, Königstuhl 17, 69117 Heidelberg, Germany*

³*ELTE Eötvös Loránd University, Institute of Physics, Pázmány Péter sétány 1/A, 1117 Budapest, Hungary*

(Received; Revised; Accepted January 4, 2022)

Submitted to ApJ

ABSTRACT

Mass accretion from the circumstellar disk onto the protostar is a fundamental process during star formation. Measuring the mass accretion rate is particularly challenging for stars belonging to binary systems, because it is often difficult to discriminate which component is accreting. DQ Tau is an almost equal-mass spectroscopic binary system where the components orbit each other every 15.8 days. The system is known to display pulsed accretion, i.e., the periodic modulation of the accretion by the components on eccentric orbit. We present multiepoch ESO/VLT X-Shooter observations of DQ Tau, with the aim to determine which component of this system is the main accreting source. We use the absorption lines in the spectra to determine the radial velocity of the two components, and measure the continuum veiling as a function of wavelength and time. We fit the observed spectra with non-accreting templates to correct for the photospheric and chromospheric contribution. In the corrected spectra we study in details the profiles of the emission lines and calculate mass accretion rates for the system as a function of orbital phase. In accordance with previous findings, we detect elevated accretion close to periastron. We measure that the accretion rate varies between $10^{-8.5}$ and $10^{-7.3} M_{\odot} \text{ yr}^{-1}$. The emission line profiles suggest that both stars are actively accreting and the dominant accretor is not always the same component, varying in few orbits.

Keywords: Young stellar objects — Spectroscopic binary stars — Circumstellar disks — Stellar accretion — Spectroscopy

1. INTRODUCTION

In the last decades, the star formation process has been investigated and studied in detail for single low-mass stars. In the scenario described by the magnetospheric accretion model (Hartmann et al. 2016), a strong magnetic field of the young star guides the accretion flow, which is responsible for the interplay between the star and the disk. Such strong magnetic field truncates the inner edge of the circumstellar disk in a region where the viscous pressure balances the magnetic pressure, called magnetospheric radius (R_M). This occurs typically at a distance of $R_M \sim 5 - 10 R_{\star}$. This single-

star accretion scenario has been confirmed by a large amount of observational evidence of classical T Tauri stars (CTTs) that support the physical mechanism of the inner disk truncation (e.g Rigliaco et al. 2012; Antonucci et al. 2014; Alcalá et al. 2014, 2017; Manara et al. 2017, 2019; Fiorellino et al. 2021). However, the single-star accretion scenario fails to describe close binary systems (with separation below 100 au), for which the presence of the other component affects the dynamics or even the presence of the circumstellar disks, and, as a consequence, the accretion process.

The current binary system accretion scenario has two main predictions (Monin et al. 2007; Tofflemire et al. 2017). First, the orbital motion clears a certain region around the two components, leading to the formation of up to three disks: two circumstellar disks, one around each component, and a circumbinary disk (CBD,

Artymowicz & Lubow 1994), which has been confirmed through observations (e.g. Andrews et al. 2011). Second, due to the dynamics of the binary system, some material from the CBD periodically forms accretion streams which fuel the circumstellar disks, if any, or directly the forming-stars (Artymowicz & Lubow 1996). Theoretical simulations by Muñoz & Lai (2016) predicts that in equal-mass binary systems, if the orbit is highly eccentric, the main accretor has a mass accretion rate up to 10 – 20 times larger than its companion, and the main accretor changes after about 100 periods, always with larger mass accretion rate. This prediction makes highly eccentric, equal-mass binaries the ideal laboratory to study the accretion and verify hydrodynamical simulations.

The double-lined spectroscopic binary DQ Tau is the archetype of the equal-mass, highly eccentric, close binary systems. It was discovered by Mathieu et al. (1997). DQ Tau is composed by two low-mass M0–M1 type CTTs that orbit each other with an orbital period of $P = 15.80158 \pm 0.00066$ days and eccentricity of 0.568 (Czekala et al. 2016). The rotational period of the stars is $T = 3.017 \pm 0.004$ days (Kóspál et al. 2018). The most recent and accurate determination of the stellar mass was given by Czekala et al. (2016), by combining the orbital solution fitted to radial velocity (RV) data and a disk model fitted to ALMA CO observations. Adopting a distance of 155 pc, they obtained $M_{*,1+2} = 1.21 \pm 0.26 M_{\odot}$. Here, we adopt the Gaia EDR3 distance of $d = 195$ pc (Bailer-Jones et al. 2021). Since the mass scales linearly with the distance (Czekala et al. 2016), the total mass of the system at 195 pc is $M_{*,1+2} = 1.52 \pm 0.33 M_{\odot}$. Using the mass ratio computed by Czekala et al. (2016), $M_2/M_1 = 0.93 \pm 0.05$, the masses of the individual components are $M_{*,1} = 0.74 M_{\odot}$ and $M_{*,2} = 0.78 M_{\odot}$. The new distance, together with constraints from the orbital solution of Czekala et al. (2016), provides a new inclination of 20.7 deg and new orbital major axis of $a = 0.142$ au.

One among the first estimates of the mass accretion rate (\dot{M}_{acc}) of DQ Tau was obtained by studying the luminosity of the boundary layer, providing $\log \dot{M}_{\text{acc}} = -7.3$ (Hartigan et al. 1995). They provided first results on its orbit and light curves, and they interpreted the accretion process of DQ Tau in the frame of the “pulsed accretion model” (Artymowicz & Lubow 1996), according to which the accretion is highly modulated by the binaries orbital motion, peaking during periastron passages, with 90% of the total mass accreted between phases $\phi = 0.7 - 1.3$. At those phases, the accretion rate increases on average by a factor of

five, in agreement with Muñoz & Lai (2016) simulations. This interpretation has been confirmed in the following DQ Tau accretion studies (e.g. Salter et al. 2010; Tofflemire et al. 2017; Kóspál et al. 2018; Muzerolle et al. 2019). However, while the on-average results confirm the model predictions, Tofflemire et al. (2017) found a complex variability from epoch to epoch, suggesting that the material accretes from the inner edge of the CBD in a more complex way than predicted by models. Accretion events near apastron were also observed and seem to be (quasi)periodic in nature.

To better understand the complex accretion process in DQ Tau system, we computed the mass accretion rate of this source by analysing the emission lines which trace accretion streams among a wide wavelength range, from the ultraviolet (UVB) to the near-infrared (NIR), for 8 epochs with high resolution spectra. In this way, we were able to study the accretion variability, and to discuss which component is accreting the most.

The structure of the paper is as follows: in Sect. 2 we report the observations and the data reduction, including telluric correction and flux calibration. In Sect. 3 we describe how we computed the radial velocity, the veiling, the extinction, the spectral type, and the disk mass of DQ Tau. In Sect. 4 we describe how we subtracted the photospheric and chromospheric contributions to our spectra, focusing on the analysis of the accretion rates. In Sect. 5 we summarize our results and draw conclusions.

2. OBSERVATIONS AND DATA REDUCTION

Observations were taken at 8 different epochs between 2012 November 18 and 2013 March 11 with the X-Shooter spectrograph on Very Large Telescope (VLT) at ESO’s Paranal Observatory in Chile (Vernet et al. 2011). X-Shooter covers simultaneously a wide wavelength range from 300 nm to 2480 nm, and the spectra are divided into three arms, the ultraviolet (UVB, 300 – 550 nm), the visible (VIS, 500 – 1020 nm), and the near-infrared (NIR, 1000 – 2480 nm). Observations of DQ Tau were performed with the narrow slits of 0.5”, 0.4”, and 0.4” in the UVB, VIS, and NIR respectively, leading to spectral resolution of $R \sim 9700, 18400$, and 11600, respectively. The exposure time in each epoch was 1220 s, 840 s, and 1200 s in the three arms, respectively.

The data are publicly available in the ESO archive^{1 2}. We downloaded data reduced with the VLT/X-Shooter pipeline, which consist of extracted, wavelength-

¹ http://archive.eso.org/wdb/wdb/adp/phase3_main/query

² <http://archive.eso.org/scienceportal/home>

Table 1. Observing log

Name	DATE OBS	HJD	Seeing [$''$]	Airmass	SNR _{UVB}	SNR _{VIS}	SNR _{NIR}	ϕ^a	β [km s ⁻¹]
(1)	(2)	(3)	(4)	(5)	(6)	(7)	(8)	(9)	(10)
Epoch 1	2012 Nov 18	2456249.29	0.70	1.46	110	184	276	0.905	7.941
Epoch 2	2012 Nov 19	2456250.14	0.64	1.59	57	113	227	0.959	7.863
Epoch 3	2012 Dec 31	2456292.21	0.83	1.72	54	169	211	0.621	-14.047
Epoch 4	2013 Jan 02	2456294.04	0.72	1.48	49	137	241	0.737	-14.496
Epoch 5	2013 Feb 05	2456328.04	0.81	1.37	138	192	230	0.889	-26.896
Epoch 6	2013 Feb 08	2456331.03	2.79	1.37	51	129	162	0.078	-27.565
Epoch 7	2013 Mar 10	2456361.04	1.79	1.93	47	124	142	0.977	-29.953
Epoch 8	2013 Mar 11	2456362.03	1.54	1.67	41	111	133	0.040	-29.869

NOTE—^aThe phase ϕ is calculated by adopting the values from Table 3 in [Czekala et al. \(2016\)](#).

calibrated and flux-calibrated 1-dimensional spectra in tabular format following the established standard for ESO science data products.

We performed the telluric correction of the VIS and NIR bands using the molecfit tool v3.0.3 ([Kausch et al. 2015a](#)). This included correction for molecular bands as O₂ and H₂O lines in VIS ([Erlick et al. 1998](#); [Newnham & Ballard 1998](#)), where strong residuals remained even after telluric correction. We computed the signal-to-noise ratio (SNR) for the spectra after discarding the noisy parts where atmospheric transmission is very low between *JHK* bands. The SNR of the spectra depends on the wavelength and on the actual seeing and airmass, being on average higher in the NIR (~ 203), than in the VIS (~ 132) and in the UVB (~ 68). Further details about the observations are reported in Tab. 1, where the seeing, airmass and SNR mean values for each epoch are listed. Tab. 1 shows also the barycentric velocity correction β , computed by using the software BARYCORRPY ([Kanodia & Wright 2018](#)). We applied the appropriate correction to each spectrum.

In order to flux calibrate our spectra, we collected multi-filter photometry for DQ Tau from the literature ([Muzerolle et al. 2019](#)) and data archives (ASAS-SN, [Shappee et al. 2014](#); [Kochanek et al. 2017](#)). The light curves of DQ Tau are plotted in Fig. 1, along with the epochs when the X-Shooter spectra were taken. We used *BVIJHK* photometry from Figure 1 for the flux calibration. For the first four epochs, we simply interpolated the available photometry for the exact observing times of the spectra. For Epoch 5, only ASAS-SN *V*-band photometry is available. So we fitted the linear relation between each band and *V*-band photometry. Then we applied this relation to the *V*-band, finding the

putative *B*-, *I*-, *J*-, *H*-, and *K*-band photometry. Lastly, no photometry in any band is available for Epochs 6, 7, and 8. To flux calibrate these spectra, we computed the phase, listed in Tab. 1, of these epochs from orbital parameters provided by [Czekala et al. \(2016\)](#), and we used the averaged data of the *V*-band for previous periods at the same phase. Then, we applied the fitted relation already used for Epoch 5 to estimate *B*-, *I*-, *J*-, *H*-, and *K*-band photometry.

We then convert our photometry from magnitudes to flux, by using Bessel zero-fluxes³. We linearly interpolated the fluxes for all the wavelength range to flux calibrate the spectra wavelength by wavelength.

The achieved flux calibration of the X-Shooter spectra is shown in Appendix A, in Fig. 13, epoch by epoch, and in Fig. 14 for all the epochs.

3. ANALYSIS

3.1. Spectral Type and Extinction

We performed the spectral typing of DQ Tau by comparing our spectra to a grid of empirical templates from G4 to M9.5 ([Manara et al. 2013](#)), that has a typical step of 1 spectral sub-class for spectral type G and K, and of 0.5 spectral sub-class for M type stars. For the comparison, we used only those observed spectra in which the two component were not resolved so that the overall system can be treated as a single star, that means Epoch 3 (see Tab. 2). We reddened the templates, and shift their flux to the one of DQ Tau in two windows of $\Delta\lambda = 5$ nm, one around $\lambda = 570$ nm, the other around

³ <http://svo2.cab.inta-csic.es/theory/fps/index.php?mode=browse&gname=Generic&asttype=>

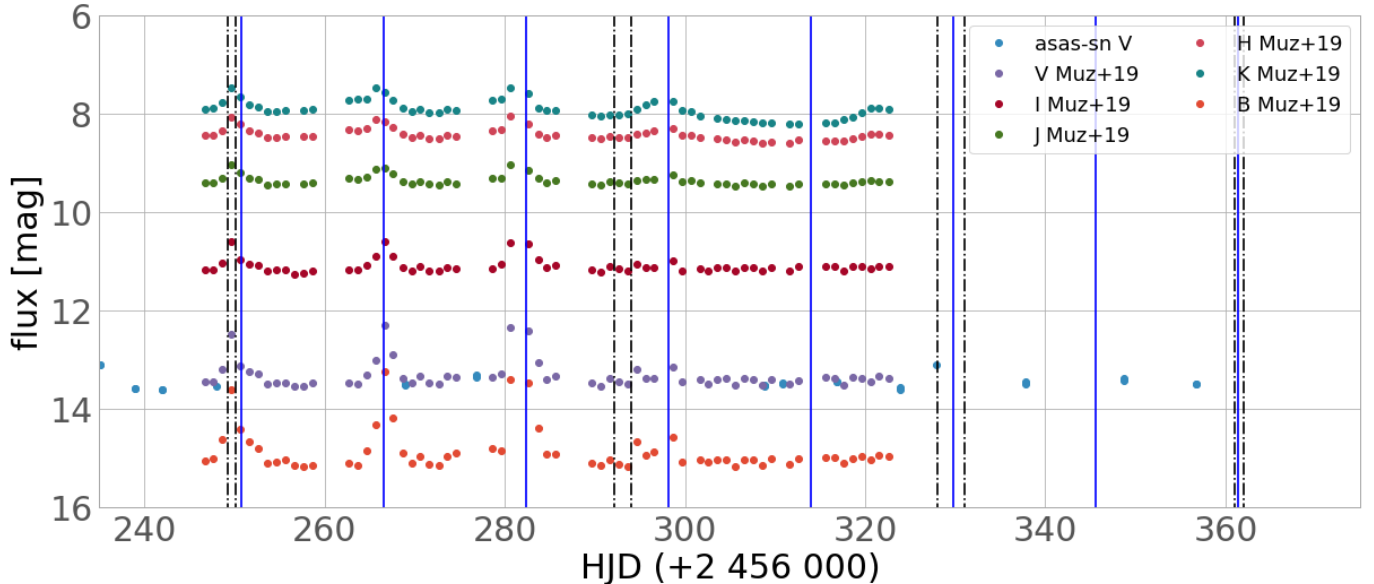


Figure 1. The light curve of DQ Tau. The epochs of the X-Shooter observations are marked with black point-dashed lines. The epochs of periastron passage are marked with blue lines. Note that Epoch 2 and Epoch 7 correspond to periastron passages. Light curves are obtained from ASAS-SN data or from Muzerolle et al. (2019) photometry, as described in the legend.

$\lambda = 1230$ nm. By varying the template and the extinction and matching the shape of the overall spectrum and the molecular features of our data with the ones of the templates, we find the best fitting spectral type for the DQ Tau system is M0, in agreement with the literature (Herbig 1977; Herczeg & Hillenbrand 2014; Czekala et al. 2016), with $A_V = 1.7$ mag. After having computed the veiling (see Sect. 3.3), we checked this spectral type by correcting the spectra for the veiling. Our best fit is still M0 type with $A_V = 1.7$ mag. This is not surprising, because the veiling is low in the visible, and increases only in the NIR, where we expect the IR-excess (see Fig. 4).

We computed the extinction towards DQ Tau in an independent way as well, with the help of the color-color diagram shown in Fig. 2, for Epoch 3, for the same reasons described above. We evaluated the needed extinction to shift the position of the DQ Tau system on the CTTs locus (Meyer et al. 1997), by using the extinction law by Cardelli et al. (1989) and $R_V = 3.1$. The resultant extinction we found is $A_V = 1.72 \pm 0.26$ mag, in agreement with the literature (e.g. Tofflemire et al. 2017), and with our spectral typing. We adopt this latter value as the interstellar extinction and $A_V = 0$ for the circumstellar extinction, because in Kóspál et al. (2018), the dips due to circumstellar extinction only cause very small changes, and only for 4.85 days in total, which corresponds to 6% of the time, which suggests all the extinction of DQ Tau is basically due to the interstellar medium.

3.2. Radial Velocity

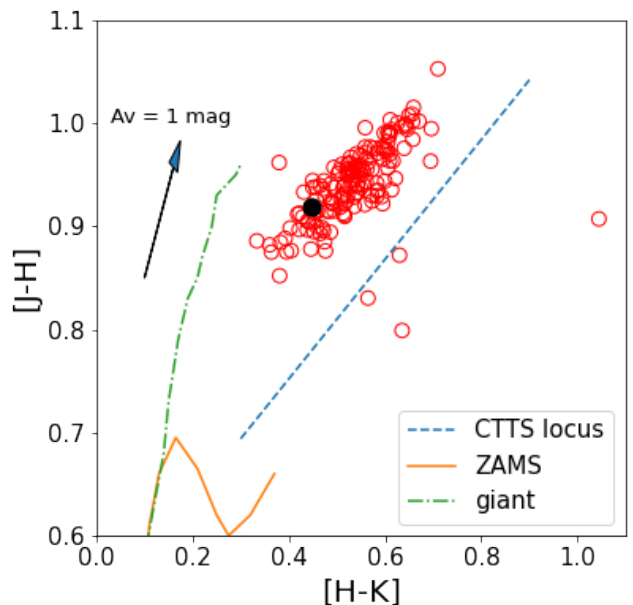


Figure 2. Color diagram of DQ Tau. Circles are data from Muzerolle et al. (2019). The black filled circle corresponds to JHK photometry for Epoch 3. Blue dashed line represent the CTTs locus. The blue arrow shows the shift for a source with 1 mag of extinction. The orange line represents the zero age main sequence, while the green dash-dotted line marks the giant branch from Koornneef (1983).

The radial velocity (RV) of DQ Tau components was measured using SAPHIRES code⁴, which determines the relative broadening functions (BFs). For a complete description of the code, we address the reader to [Tofflemire et al. \(2019\)](#). To compute the BFs and RVs, high-resolution empirical templates of non-accreting Class III spectra were used ([Manara et al. 2013](#)). As a first step, we found the best-fit template spectrum that matches DQ Tau by determining BFs among the various spectral types ranging from K7 to M3.5. We used only the VIS and NIR spectra, where the continuum and absorption lines are detected with higher SNR than in the UVB. Among the various spectral types in both VIS and NIR, the BF obtained by using M0 template (TYC 7760-283-1) showed the best fit with our spectra. To measure the RVs, we only utilized the VIS, because of their higher resolution and relatively well-corrected telluric absorption features. In addition to the best BFs, the M0 template shows the smallest uncertainties of RVs for all observed epochs among all the different spectral types. Consequently, we adopted the M0 template to measure the RVs of DQ Tau. We note that the M0 template is also compatible with the spectral type we obtained in Sect. 3.1

The RV of the M0 template spectrum was measured by fitting the BFs with a synthetic spectrum ($T_{\text{eff}} = 3750$ K, $\log g = 1$, and solar abundance; [Coelho et al. 2005](#)). We obtained $RV = 6.26 \pm 1.52$ km s⁻¹. The barycentric velocity of the template spectrum was computed by using barycorrpy ([Kanodia & Wright 2018](#)) as 2.74 km s⁻¹. The template spectrum was therefore shifted by RV and barycentric velocity. The resultant velocity corrected spectrum was used to measure the RVs of DQ Tau.

RVs of DQ Tau were computed by considering 22 fitting regions with about 100 Å wavelength intervals for each epoch. We excluded wavelength ranges where emission lines and strong residuals from telluric absorption lines were present. The mean and standard deviation values are adopted as RV and its uncertainty, respectively. In most epochs, the BFs were double peaked, so we could fit separately the RVs of the two components in all epochs, except for Epoch 3. For Epoch 3, the BF is single-peaked, so the RVs of the two stars must be identical within the uncertainties, so, for this epoch, we give the same value for both stars in Tab. 2, where results are listed. These values are plotted in Fig. 3.

The top panel in Fig. 3 shows the RVs we measured and the ones from [Czekala et al. \(2016\)](#). To calculate

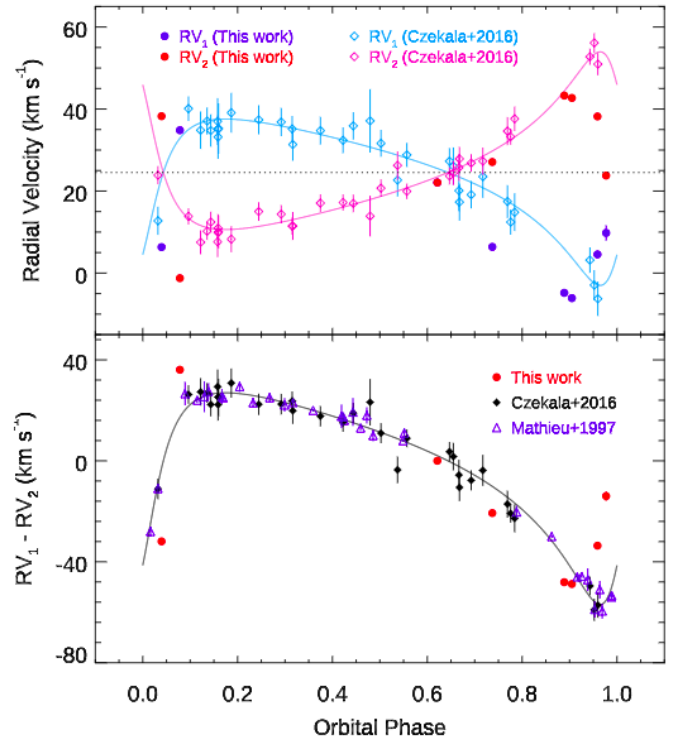


Figure 3. *Top:* Radial velocity of DQ Tau as a function of orbital phase. Blue and red symbols indicate RVs measured in this study (Tab. 2). Sky blue and pink symbols and solid lines present the RVs and orbital solution from [Czekala et al. \(2016\)](#), respectively. *Bottom:* Radial velocity differences as a function of orbital phase. Black and red symbols indicate values from [Czekala et al. \(2016\)](#) and this work. Blue symbol represents the data from [Mathieu et al. \(1997\)](#). The uncertainty smaller than the symbol size is not presented.

the orbital phase, we adopted the orbital solutions from [Czekala et al. \(2016\)](#), also shown in the figure as solid lines. The phase coverage of our 8 measurements are not sufficient to determine a Keplerian solution independently, but our results agree with those from [Czekala et al. \(2016\)](#). There is a slight offset between the absolute values of our RVs and those from [Czekala et al. \(2016\)](#), but as shown in the bottom panel of Fig. 3, the RV difference of the two components are well consistent with previous studies ([Czekala et al. 2016](#); [Mathieu et al. 1997](#)) based on data observed with different telescopes and instruments.

3.3. Veiling

In order to subtract the chromospheric and photospheric contribution from the DQ Tau spectra, we first evaluated the veiling of the source. We first normalized the observed spectra ($F_{\nu, \text{obs}}$) and the template spectrum

⁴ <https://github.com/tofflemire/saphires>

Table 2. Radial Velocity and Accretion Parameters.

Epoch	ϕ	RV ₁	RV ₂	$\log(L_{\text{acc}}/L_{\odot})$	$\log(\dot{M}_{\text{acc}}/M_{\odot}/\text{yr})$	Number of
		km s ⁻¹	km s ⁻¹			detected lines
1	0.90	-6.11 ± 0.27	42.70 ± 0.42	-0.144 ± 0.032	-7.313 ± 0.032	37
2	0.96	4.56 ± 0.37	38.19 ± 0.44	-0.138 ± 0.039	-7.307 ± 0.039	36
3	0.62	22.08 ± 0.14	22.08 ± 0.14	-1.380 ± 0.034	-8.549 ± 0.034	20
4	0.74	6.38 ± 0.40	27.08 ± 0.48	-1.093 ± 0.032	-8.262 ± 0.032	25
5	0.89	-4.82 ± 0.73	43.28 ± 0.26	-0.423 ± 0.031	-7.592 ± 0.031	37
6	0.08	34.83 ± 0.52	-1.24 ± 0.68	-0.744 ± 0.035	-7.913 ± 0.035	28
7	0.98	9.79 ± 1.82	23.78 ± 0.14	-0.508 ± 0.024	-7.678 ± 0.024	34
8	0.04	6.33 ± 0.33	38.25 ± 0.83	-0.793 ± 0.046	-7.962 ± 0.046	34

NOTE—The orbital phase (ϕ) is computed with respect the nearest previous periastron assuming parameters from [Czekala et al. \(2016\)](#).

($F_{\nu,\text{temp},0}$), then applied a veiling V to the template:

$$F_{\nu,\text{temp,veiled}} = \frac{F_{\nu,\text{temp},0} + V}{1 + V}. \quad (1)$$

We call the V parameter *continuum veiling* in accordance with the usual practice in the literature ([Basri & Batalha 1990](#)), while acknowledging that line veiling may contribute to the measured value. It was suggested that emission lines may cause additional veiling (on top of the veiling caused by continuum emission) by [Folha & Emerson \(1999\)](#). [Dodin & Lamzin \(2012\)](#) wrote that narrow emission lines in the post-shock region contribute to the veiling of the photospheric absorption lines and concluded that this contribution is most significant for moderately accreting CTTs. Therefore, this could potentially be important for DQ Tau. [Rei et al. \(2018\)](#) studied high resolution spectra of three T Tauri stars and found strongly line-dependent veiling: veiling was larger if measured from stronger photospheric lines and lower or absent from weaker lines. They concluded that the best estimate for the true value of the continuum veiling can be obtained by measuring the weakest photospheric lines with equivalent widths (EWs) down to 10 mÅ, and lines with EW above 100 mÅ may already suffer from line veiling.

To find out if line veiling is significant in DQ Tau, we checked the EWs of the photospheric absorption lines we used for our veiling calculation. We found that all of these lines have $\text{EW} < 100$ mÅ in epochs 1, 2, and 5, and only 1 – 8 lines have $\text{EW} > 100$ mÅ in the other epochs. We found no correlation between the measured veiling and the EWs in any of the epochs. Because we used only lines with $\text{EW} < 100$ mÅ for our veiling calculations (with a few exceptions), according to [Rei et al. \(2018\)](#), our result should give the best possible estimate of the true level of the continuum veiling. As we see no dependence of the veiling on EW, we can conclude

that in the EW range we use for our calculations, line veiling is negligible. For each epoch, we measured the veiling by studying suitable wavelength ranges around the absorption lines, that are sensitive to the veiling itself. We varied the veiling values between 0 and 3, in steps of 0.01, and computed the χ^2 between the veiled template $F_{\nu,\text{temp,veiled}}$ and the DQ Tau spectrum $F_{\nu,\text{obs}}$, choosing the veiling value which minimizes the χ^2 . In the following analysis we use the same veiling for the two components, assuming that in each epoch the primary and the secondary both suffer the same veiling. This is not necessarily true, but the limited spectral resolution of X-Shooter, compared to the relatively narrow photospheric absorption lines, and the rather low SNR of the individual absorption lines did not allow us to measure the veiling separately for the two components. Fig. 4 shows the veiling values measured in 5 nm wide wavelength ranges for selected absorption lines. We discarded portions of the spectra where strong residuals of telluric absorption are present. To better outline the general trend how the veiling varies with wavelength and time, we calculated the median of the measured veiling values in 200 nm wide bins. We plotted these median values in black in Fig. 4 which reveals two main trends: (i) in Epochs 2, 3, 4, 6, 7 and 8, the veiling is almost constant in the UVB and VIS bands, and increasing in the NIR; (ii) in Epochs 1 and 5, the veiling is constant only in the visible, while it increases both towards shorter and longer wavelengths.

In Fig. 5, we show the median veiling as a function of the orbital phase. This figure shows that the veiling varies significantly with the orbital phase, being larger immediately before the periastron both in the NIR and VIS, and with the orbit, being larger for Epochs 1 and 2, which belong to the same orbit, than for other epochs, which belong to a subsequent orbit.

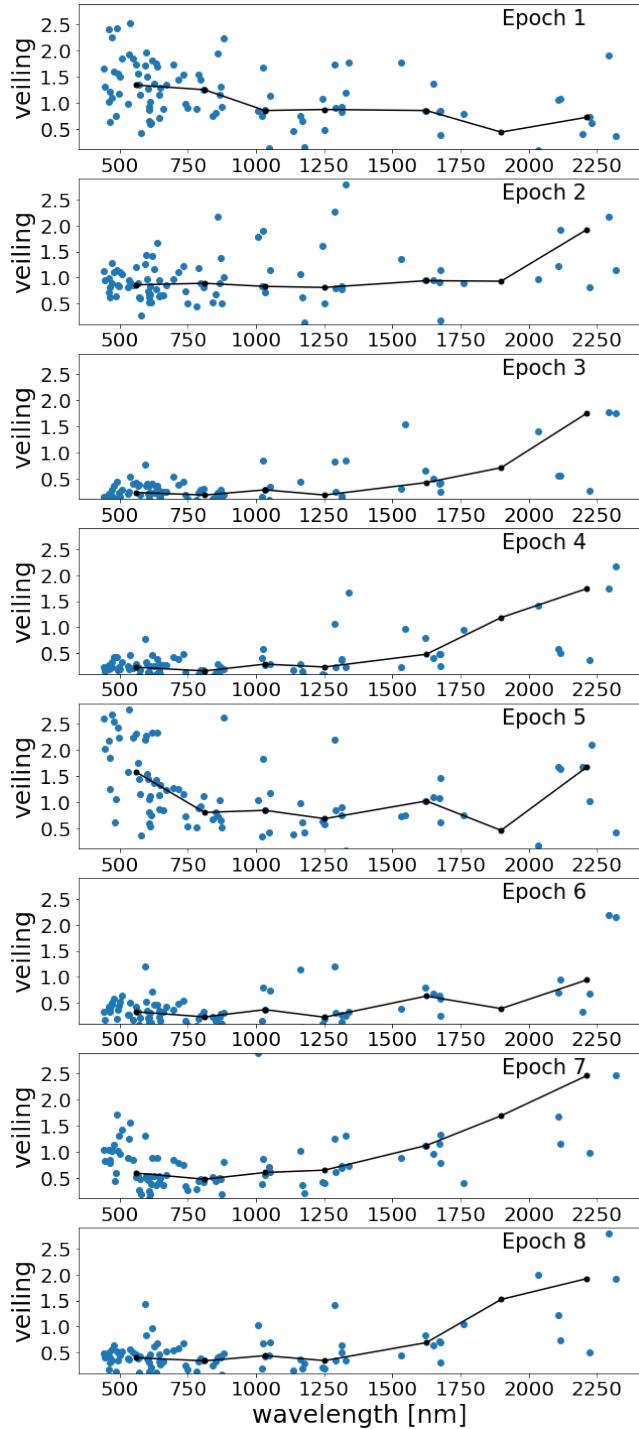


Figure 4. Veiling as a function of the wavelength for each epoch. Blue dots are results of the analysis, black dots correspond to median values in 200 nm wide bins.

4. ACCRETION IN DQ TAU

DQ Tau spectra display several emission lines that trace the accretion process. The strength of these lines varies with the orbital phase, and these can be used to

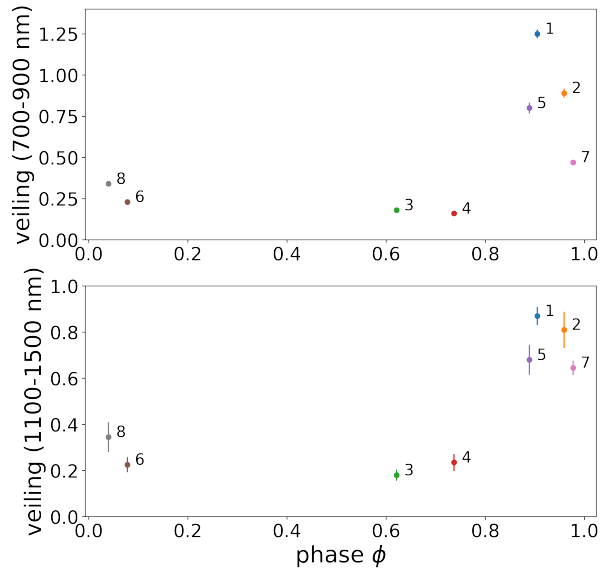


Figure 5. Median veiling values in the optical (top) and near-infrared (bottom) wavelength ranges. Different colors indicate different epochs. Uncertainties smaller than the symbol size are not presented.

calculate the accretion luminosity and the mass accretion rate of the system. In the following, we describe in details the various steps of this procedure, and the relative analysis we performed.

4.1. Correction for Photospheric and Chromospheric Contributions

The observed accretion lines of DQ Tau are contaminated by the photospheric and chromospheric contributions of each component. According to the spectral typing and the radial velocity analysis, the DQ Tau system is consistently described by two M0 stars. Under the assumption that stars of the same spectral type have similar chromospheric contribution, we fitted both components with the same template, as described below.

For this procedure, we used normalized spectra. The normalization of the spectra was performed considering wavelength ranges of 5 nm. For each wavelength range, we computed the median value of the spectrum, discarding the strong emission lines. We then fitted these median values with a polynomial of second order, and divided the spectra for the fitted line.

For each epoch, we normalized two spectra of the TYC 7760-283-1 star, an M0 Class III (Manara et al. 2013) also known as V1249 Cen, each shifted to the radial velocity computed in Sect. 3.2. Then, we summed the two spectra and normalized them again. Hence, we veiled the new template using the values estimated in Sect. 3.3. We subtracted the flux of this template from each line of the normalized DQ Tau spectra which traces

the accretion, so that the remaining emission line is completely due to the accretion process.

4.2. Measuring Emission Line Fluxes

After we subtracted the photospheric and chromospheric contributions of the binary components for each epoch, we calculated the fluxes of the accretion tracer emission lines in the following way. First, we fitted a linear curve to the local continuum in a wavelength range of $\Delta\lambda = 2$ nm, centered on the emission line wavelength λ_0 . We modified slightly this range, if needed, taking the one most suitable for each line, for example, avoiding other emission lines, if present, or telluric absorption lines. The line flux was determined by subtracting the local continuum from the spectra and integrating it over the line. We computed the noise of the line by multiplying the standard deviation of the local continuum (RMS) for the element of wavelength between two pixels $\Delta\lambda$, and multiplying by the square root of the number of pixels within the wavelength range (N_{pix}). We considered a line detected when its $SNR > 3$. For those lines that are detected in at least one epoch, we estimated the upper limits in the other epochs as three times the noise:

$$F_{\text{line}}^{upp} = 3 \times (\sqrt{N_{pix}} \times RMS \times \Delta\lambda). \quad (2)$$

Results are shown in Tab. 3.

4.3. Accretion luminosity and mass accretion rate

In order to estimate the accretion luminosity of DQ Tau, we used the most recent empirical relations between the lines that trace accretion (L_{line}) and the accretion luminosity itself (Alcalá et al. 2017):

$$\log(L_{\text{acc}}/L_{\odot}) = a_{\text{line}} \log(L_{\text{line}}/L_{\odot}) + b_{\text{line}}, \quad (3)$$

where a_{line} and b_{line} are coefficients that vary with the line, and $L_{\text{line}} = 4\pi d^2 F_{\text{line}}$ is the luminosity of the line. The error on L_{line} was computed by using the error propagation formula, considering the error on the distance, and on the line flux. The error on F_{line} was computed in the same way, considering the error on L_{line} , and on a, b coefficients. We estimated the accretion luminosity for every line from Tab. 3, and used the mean weighted value of L_{acc} derived from these lines as the best estimate for L_{acc} for each epoch. Errors on L_{acc} are computed by dividing the standard deviation of L_{acc} computed for every line detected per the square root of the number of used lines. Results are shown in Tab. 2.

We computed the mass accretion rate \dot{M}_{acc} using the relation:

$$\dot{M}_{\text{acc}} \sim \left(1 - \frac{R_{\star}}{R_{\text{in}}}\right)^{-1} \frac{L_{\text{acc}} R_{\star}}{GM_{\star}}, \quad (4)$$

where R_{in} is the inner-disk radius which we assume to be $R_{\text{in}} \sim 5R_{\star}$ (Hartmann et al. 1998), $M_{\star} = 1.52 M_{\odot}$ and $R_{\star} = 2.58 R_{\odot}$ are the mass and radius for the overall system derived by Czekala et al. (2016) and scaled to $d = 195$ pc. We note that if we use mass and radius of a single star, being the two components of DQ Tau almost equals ($M_2/M_1 = 0.93 \pm 0.05$), the factor of two will be in both the numerator and the denominator in Eq. 4, not affecting final results. The error on \dot{M}_{acc} is computed as for L_{acc} . Being \dot{M}_{acc} proportional to L_{acc} , the error for each epoch is the same for both L_{acc} and \dot{M}_{acc} . Indeed, because we are interested in the variability of \dot{M}_{acc} , we have taken into account only the error due to the accretion variability, considering the stellar parameters fixed. Results are listed in Tab. 2. However, the absolute values of the mass accretion rate is affected also by the uncertainties on the stellar parameters, and we will do this when comparing our results to other works. In this latter case, the error results to be 0.45 dex.

Both L_{acc} and \dot{M}_{acc} are shown as a function of orbital phase in Fig. 6. We see that Epochs 3 and 4, the measurements taken closest to the apastron, show the smallest L_{acc} and \dot{M}_{acc} . On the contrary, epochs between $\phi = 0.8 - 1.0$ show significantly elevated accretion rates. Our results that the accretion depends on the orbital phase and is highest nearby periastron support previous observational and numerical results in the literature for DQ Tau and for eccentric binary systems in general (e.g. Mathieu et al. 1997; Günther & Kley 2002a; Salter et al. 2010; D’Orazio et al. 2013; Farris et al. 2014a; Muñoz & Lai 2016; Tofflemire et al. 2017; Kóspál et al. 2018; Muzerolle et al. 2019). This is in agreement with the hypothesis that the accretion flow of DQ Tau can be explained by the “pulsed accretion model” (Artymowicz & Lubow 1996), according to which the accretion is highly modulated by the binaries orbital motion, peaking during periastron passages.

It is worth considering the system’s geometry when interpreting the line flux variations because in theory, these can be caused by rotational modulation as well (e.g., Kurosawa et al. 2008; Kurosawa & Romanova 2013; Romanova & Owocki 2016). The inclination of the rotational axis of the stars in the DQ Tau binary is not known. If we assume that the stars’ equator is coplanar with the disk, then the DQ Tau system is viewed nearly pole-on ($i = 20.7$ deg), therefore we do not expect significant rotational modulation. For instance, numerical simulations by Kurosawa et al. (2008) suggest that the equivalent width of emission lines only change by up to a factor of 1.5 for $i = 10$ deg and up to a factor of 2.5 for high inclination ($i = 60 - 80$ deg)

Table 3. Observed fluxes of accretion tracers after subtracting the photospheric and chromospheric contribution.

Element	λ nm	F_{line}^1 $10^{-14} \frac{\text{erg}}{\text{s cm}^2}$	F_{line}^2	F_{line}^3	F_{line}^4	F_{line}^5	F_{line}^6	F_{line}^7	F_{line}^8
H3(H α)	656.28	382.554 \pm 0.523	558.038 \pm 0.802	128.549 \pm 0.332	160.253 \pm 0.288	301.567 \pm 0.333	396.943 \pm 0.317	354.495 \pm 0.412	219.908 \pm 0.273
H4(H β)	486.13	42.697 \pm 0.148	59.401 \pm 0.130	4.981 \pm 0.099	6.686 \pm 0.106	29.826 \pm 0.137	18.946 \pm 0.116	24.077 \pm 0.116	13.795 \pm 0.105
H5(H γ)	434.05	15.843 \pm 0.445	21.766 \pm 0.150	1.367 \pm 0.059	2.086 \pm 0.065	7.839 \pm 0.196	5.126 \pm 0.080	8.499 \pm 0.087	5.796 \pm 0.077
H6(H δ)	410.17	9.645 \pm 0.103	13.923 \pm 0.068	0.627 \pm 0.030	1.202 \pm 0.034	4.008 \pm 0.044	2.512 \pm 0.036	4.799 \pm 0.041	3.400 \pm 0.036
H7(H ϵ)	397.01	10.882 \pm 0.069	14.144 \pm 0.049	0.855 \pm 0.021	1.486 \pm 0.025	4.988 \pm 0.034	2.741 \pm 0.022	5.065 \pm 0.027	3.483 \pm 0.022
H8	388.90	4.905 \pm 0.131	7.765 \pm 0.061	0.381 \pm 0.007	0.761 \pm 0.011	1.884 \pm 0.048	1.436 \pm 0.008	2.553 \pm 0.025	1.919 \pm 0.016
H9	383.54	4.542 \pm 0.197	5.880 \pm 0.103	0.195 \pm 0.007	0.467 \pm 0.009	1.605 \pm 0.085	0.972 \pm 0.014	1.897 \pm 0.038	1.368 \pm 0.021
H10	379.79	3.479 \pm 0.102	4.395 \pm 0.039	0.124 \pm 0.006	0.312 \pm 0.007	1.236 \pm 0.039	0.674 \pm 0.012	1.439 \pm 0.019	0.923 \pm 0.011
H11	377.06	2.541 \pm 0.114	3.152 \pm 0.048	0.123 \pm 0.006	0.292 \pm 0.008	0.812 \pm 0.034	0.522 \pm 0.007	1.044 \pm 0.016	0.689 \pm 0.010
H12	375.02	1.756 \pm 0.101	2.177 \pm 0.048	0.059 \pm 0.004	0.176 \pm 0.005	0.652 \pm 0.043	0.370 \pm 0.006	0.789 \pm 0.019	0.437 \pm 0.012
H13	373.44	1.863 \pm 0.125	1.651 \pm 0.067	0.039 \pm 0.002	0.109 \pm 0.005	0.573 \pm 0.047	0.273 \pm 0.008	0.629 \pm 0.029	0.291 \pm 0.013
H14	372.19	1.780 \pm 0.102	1.427 \pm 0.029	0.022 \pm 0.003	0.061 \pm 0.004	0.692 \pm 0.038	0.234 \pm 0.006	0.522 \pm 0.016	0.172 \pm 0.012
H15	371.20	0.610 \pm 0.151	0.508 \pm 0.110	0.041 \pm 0.004	0.076 \pm 0.009	0.239 \pm 0.059	0.122 \pm 0.019	0.239 \pm 0.043	0.105 \pm 0.021
Pa5(Pa β)	1281.81	69.714 \pm 0.717	73.728 \pm 0.557	4.930 \pm 0.445	9.130 \pm 0.439	60.821 \pm 0.301	33.397 \pm 0.606	39.672 \pm 0.541	18.321 \pm 0.477
Pa6(Pa γ)	1093.81	49.409 \pm 0.922	49.751 \pm 2.615	3.597 \pm 0.867	6.103 \pm 0.704	39.439 \pm 1.187	18.951 \pm 1.026	26.125 \pm 0.549	12.532 \pm 0.434
Pa7(Pa δ)	1004.94	33.388 \pm 0.821	32.848 \pm 0.902	< 1.261	1.946 \pm 0.462	36.847 \pm 0.839	12.547 \pm 0.538	21.529 \pm 0.753	11.423 \pm 0.779
Pa9	922.90	20.552 \pm 0.327	12.120 \pm 0.234	< 0.683	1.168 \pm 0.167	17.403 \pm 0.277	3.982 \pm 0.209	8.724 \pm 0.221	3.680 \pm 0.171
Pa10	901.49	19.805 \pm 0.239	7.957 \pm 0.288	< 1.359	< 0.970	14.578 \pm 0.311	2.409 \pm 0.285	6.022 \pm 0.321	1.933 \pm 0.276
Br7(Br γ)	2166.12	21.706 \pm 0.586	17.710 \pm 0.593	< 1.047	1.217 \pm 0.288	14.483 \pm 0.348	7.181 \pm 0.595	8.520 \pm 0.347	2.905 \pm 0.226
HeI	402.62	0.490 \pm 0.027	0.772 \pm 0.017	< 0.045	0.073 \pm 0.017	0.210 \pm 0.013	0.123 \pm 0.014	0.213 \pm 0.013	0.172 \pm 0.012
HeI	447.15	1.635 \pm 0.242	2.336 \pm 0.134	< 0.378	0.400 \pm 0.122	0.887 \pm 0.164	0.605 \pm 0.115	0.924 \pm 0.109	0.765 \pm 0.104
HeI	471.31	0.312 \pm 0.045	0.355 \pm 0.053	< 0.199	< 0.176	0.209 \pm 0.034	< 0.158	< 0.162	0.154 \pm 0.046
HeI+FeI	492.19	7.896 \pm 0.099	2.917 \pm 0.133	< 0.457	< 0.414	5.675 \pm 0.109	< 0.426	1.204 \pm 0.119	0.615 \pm 0.119
HeI	501.57	7.864 \pm 0.114	2.846 \pm 0.128	< 0.456	< 0.408	5.966 \pm 0.119	< 0.402	1.143 \pm 0.119	0.380 \pm 0.112
HeI	587.56	7.670 \pm 0.359	9.430 \pm 0.393	< 1.649	2.252 \pm 0.566	3.035 \pm 0.425	3.419 \pm 0.457	5.243 \pm 0.346	3.727 \pm 0.446
HeI	667.82	4.419 \pm 0.203	4.465 \pm 0.256	< 0.900	< 0.845	2.434 \pm 0.163	1.274 \pm 0.241	2.587 \pm 0.262	1.713 \pm 0.236
HeI	706.52	2.732 \pm 0.256	2.677 \pm 0.306	< 1.086	< 1.020	1.237 \pm 0.205	< 0.950	0.944 \pm 0.291	< 1.003
HeII	468.58	0.366 \pm 0.054	0.836 \pm 0.053	< 0.192	< 0.171	0.297 \pm 0.044	0.255 \pm 0.050	0.287 \pm 0.052	0.278 \pm 0.046
CaII(K)	393.37	8.177 \pm 0.158	6.016 \pm 0.064	0.451 \pm 0.010	0.720 \pm 0.013	4.227 \pm 0.073	1.255 \pm 0.012	2.333 \pm 0.032	1.303 \pm 0.015
CaII(H)	396.85	10.67 \pm 0.056	13.810 \pm 0.047	0.876 \pm 0.013	1.452 \pm 0.016	4.989 \pm 0.034	2.733 \pm 0.018	4.984 \pm 0.022	3.374 \pm 0.020
CaII	849.80	46.784 \pm 0.239	12.508 \pm 0.241	< 0.676	< 0.560	44.201 \pm 0.201	1.393 \pm 0.202	11.62 \pm 0.213	3.794 \pm 0.155
CaII	854.21	42.254 \pm 0.127	15.632 \pm 0.114	< 0.562	< 0.452	42.988 \pm 0.115	< 0.487	11.92 \pm 0.179	0.612 \pm 0.175
CaII	866.21	39.072 \pm 0.221	15.205 \pm 0.210	< 1.145	< 0.886	40.766 \pm 0.168	< 0.844	12.234 \pm 0.321	1.487 \pm 0.273
NaI	589.00	2.162 \pm 0.219	1.157 \pm 0.214	< 0.793	< 0.821	2.363 \pm 0.270	< 0.678	< 0.518	< 0.701
NaI	589.59	1.260 \pm 0.288	< 0.869	< 0.860	< 0.885	1.483 \pm 0.345	< 0.684	< 0.527	< 0.664
OI	777.31	8.276 \pm 0.275	3.752 \pm 0.297	< 1.197	< 0.974	5.466 \pm 0.225	< 0.944	2.234 \pm 0.335	1.469 \pm 0.310
OI	844.64	19.353 \pm 0.649	19.197 \pm 0.380	< 1.828	2.259 \pm 0.493	17.341 \pm 0.462	7.388 \pm 0.462	8.757 \pm 0.511	4.772 \pm 0.471

Reported flux values are not dereddened.

models, while we observe significantly larger variations in DQ Tau despite its low inclination. Moreover, the line variations observed in DQ Tau are periodic with the orbital period of the binary and not with the rotational period of the stars. The ratio between the system's orbital period (15.80158 ± 0.00066 d) and rotational period (3.017 ± 0.004 d) is 5.2375 ± 0.0069 , which is far from any possible low-order resonances (Kóspál et al. 2018). Therefore, we can exclude with high confidence that the axial rotation of the components is synchronized with the orbital motion and changes periodic with the rotational period cannot be confused with changes that are periodic with the binary's orbital period. In conclusion, the observed line flux variations are unlikely to be explained by rotational modulation.

Looking more in detail at Fig. 6, we note that, when detected, the He I at 501.6 nm and He I+Fe I blend at 492 nm give accretion rates systematically larger than the other lines. On the contrary, the Paschen series usually provide lower accretion rates, especially in Epochs 3,

4, 6, and 8. The final errors on the $\log L_{\text{acc}}$ values of individual lines are in the range of 0.17 to 0.73, having a typical uncertainty of 0.33 dex in L_{acc} . Fig. 6 shows that the observed differences in accretion luminosity often exceeds these, hinting for a physical reason behind, i.e., that different lines trace different parts of the accretion flow with different physical conditions. We will discuss this point in detail in Sect. 4.8. We note that not all epochs have the same lines detected. To minimize the effect of these uncertainties, we calculated the mean weighted value as the best estimate for the accretion rate.

4.4. Comparing the Continuum Veiling and the Mass Accretion Rate

The continuum veiling values plotted in Fig. 5 and the accretion rates plotted in Fig. 6 show a similar trend with the orbital phase. Both veiling and accretion rates increase close to periastron. Epochs 1 and 2 display the maximal veiling and maximal accretion rate as well

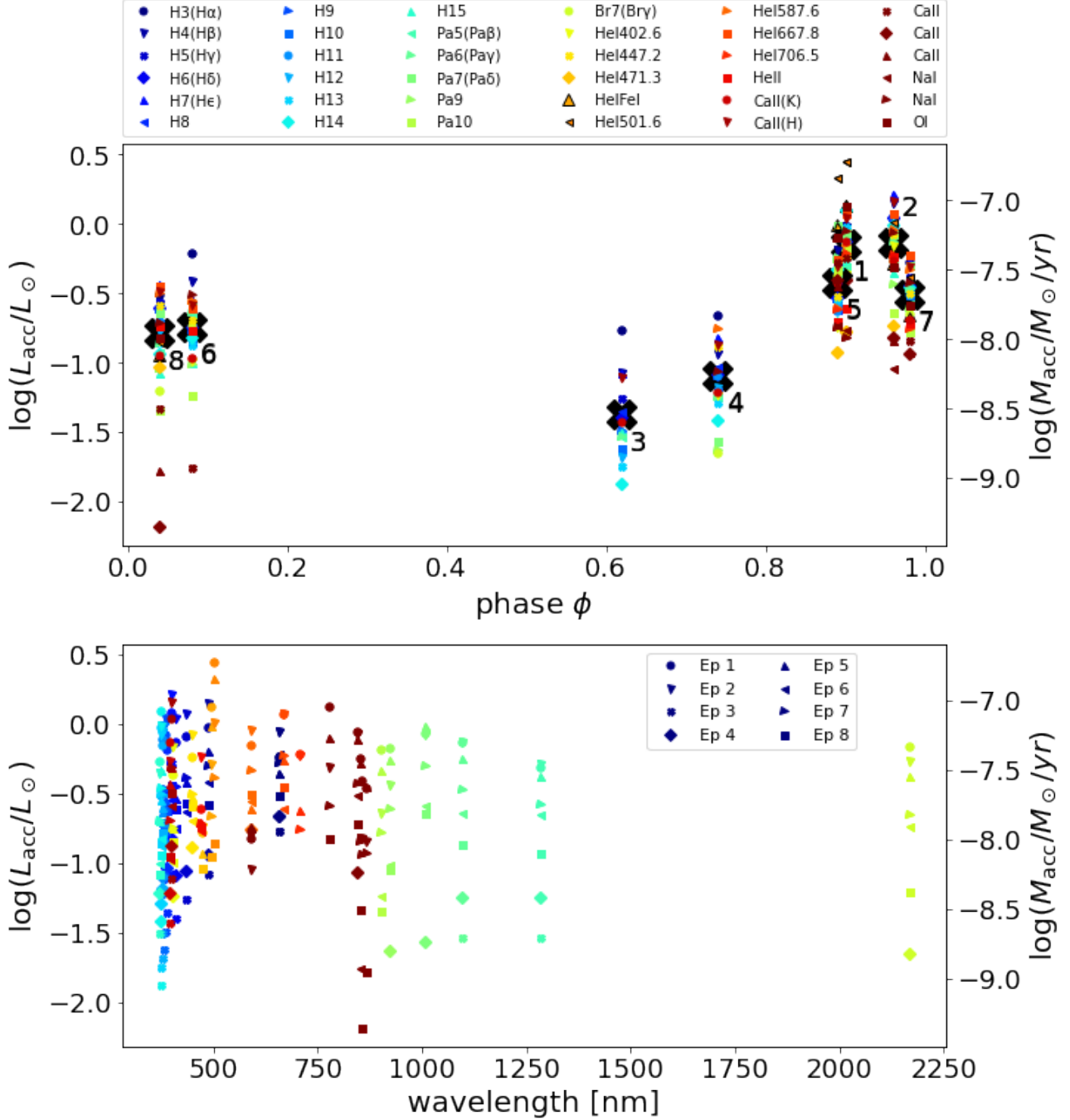


Figure 6. Accretion luminosity and mass accretion rate as a function of the orbital phase (top) and as a function of the wavelength (bottom). Each symbol indicates a different accretion tracer or epoch, as described in the legends.

during our monitoring. In the following, we want to compare our results on DQ Tau with other sources in Taurus, to verify whether this relation between the mass accretion rate and the continuum veiling is peculiar of DQ Tau or general for the Taurus star forming region. For this purpose, we plot in Fig. 7 the mass accretion rate as a function of the median veiling in the visible for a sample in Taurus (black filled dots; Muzerolle et al.

1998, rescaled to 195 pc), and for DQ Tau (red filled dots). We note that $\log M_{\text{acc}}$ of DQ Tau increases almost linearly with the continuum veiling. The figure shows that the data points for DQ Tau match the general trend outlined in Muzerolle et al. (1998).

4.5. Comparing DQ Tau with Single Accretors

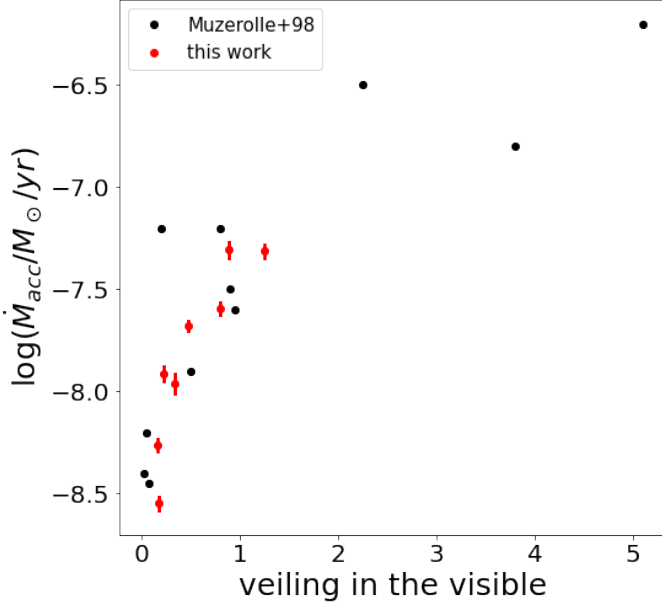


Figure 7. Mass accretion rate as a function of the continuum veiling in the visible.

During periastron, the DQ Tau components are known to approach each other to within $8 R_{\star} \sim 13 R_{\odot}$, which means that their magnetospheres merge (Salter et al. 2010). This may mean that single circumstellar disks, if present, would be disrupted by the magnetosphere during periastron, and, eventually, the accretion columns can generate directly from the CBD to the stars. Therefore, in terms of the magnetospheric accretion scenario, the DQ Tau system probably can be considered as a single star when the system is close to (or at) periastron. To verify this, we compared DQ Tau with the most recent CTTs surveys in Lupus, Chamaeleon I, NGC1333, and Taurus (Alcalá et al. 2019; Manara et al. 2019; Fiorellino et al. 2021; Alcalá et al. 2021, respectively) in Fig. 8. We plotted DQ Tau L_{acc} and \dot{M}_{acc} total values for the two stars together, at a place that corresponds to the total luminosity and mass of the two stars, respectively. We find that, in general, the accretion rates of DQ Tau (red filled diamonds) are in agreement with typical ranges of values of single CTTs with the same stellar luminosity and mass. While L_{acc} perfectly matches CTTs distributions in the $\log L_{\text{acc}} - \log L_{\star}$ diagram, the \dot{M}_{acc} of DQ Tau lies in the lower part of the $\log \dot{M}_{\text{acc}} - \log M_{\star}$ diagram. In particular, the \dot{M}_{acc} is compatible with the \dot{M}_{acc} distribution of ~ 2 Myr star-forming regions Chamaeleon I and Lupus for all the epochs. Thus, our results show that DQ Tau is accreting with a rate compatible with single stars with similar stellar parameters even when it is accreting less, nearby the apastron. This

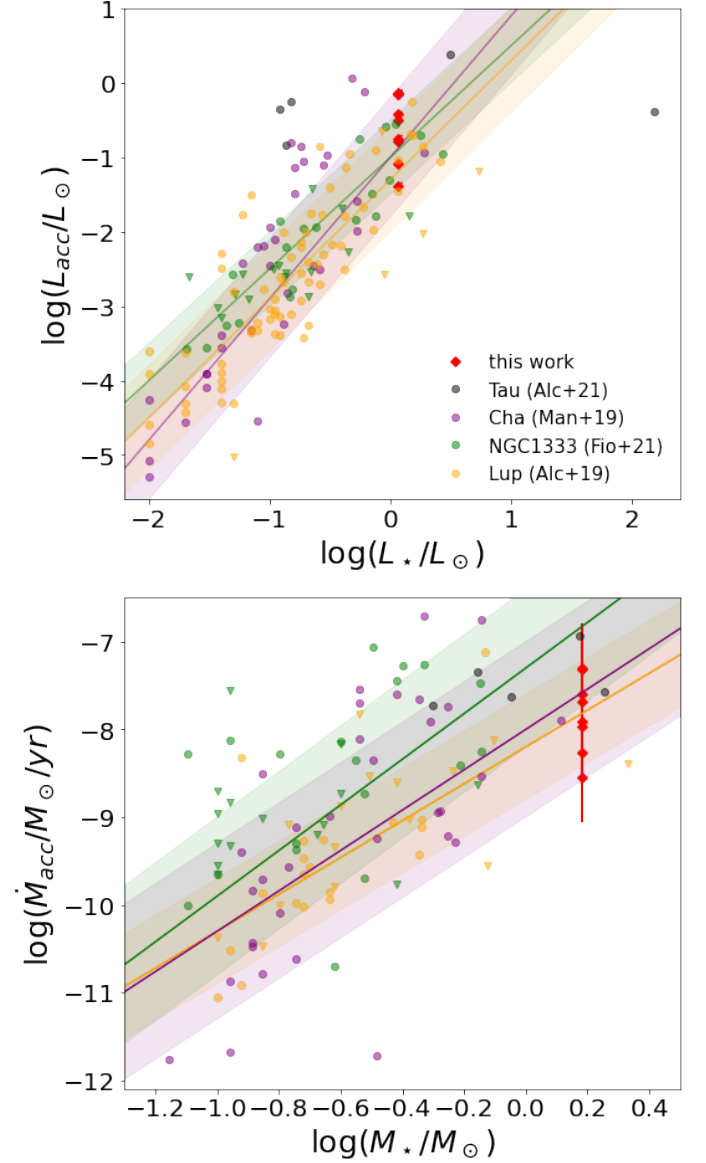


Figure 8. *Top:* Accretion luminosity versus stellar luminosity. *Bottom:* Mass accretion rate versus stellar mass. In both panels, DQ Tau results are shown in red, and the Chamaeleon I, Lupus, NGC 1333, and Taurus CTTs samples (Alcalá et al. 2019; Manara et al. 2019; Fiorellino et al. 2021; Alcalá et al. 2021) are shown together with their fits (Fiorellino et al. 2021) with the colors described in the legend.

result seems to confirm the hypothesis that we can study the \dot{M}_{acc} on DQ Tau as it was a single star.

4.6. Accretion Variability over the Binary Orbit

To study the accretion variability over the binary orbit, we compare our \dot{M}_{acc} estimates with results from previous literature, after scaling them to the distance we adopt of 195 pc. We plot in Fig. 9 the mass accre-

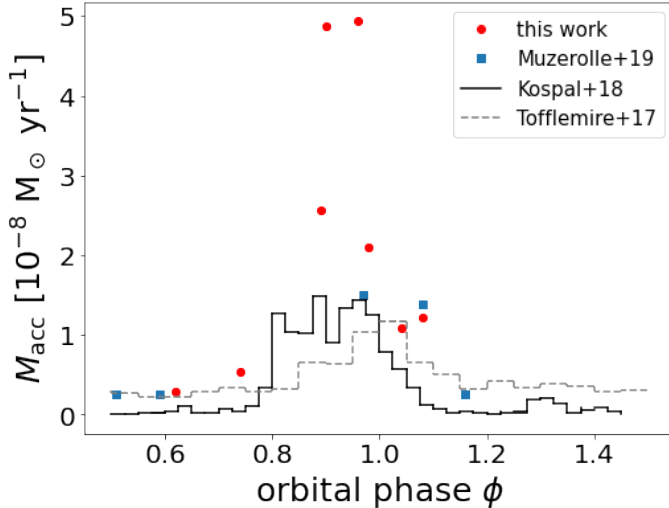


Figure 9. Mass accretion rate of DQ Tau versus phase.

tion rate as a function of the orbital phase. As described in Sect. 4.3, we used spectroscopic data and empirical relations between F_{line} and L_{acc} , to compute \dot{M}_{acc} . Our results are shown with red filled circles. The same approach was used by Muzerolle et al. (2019), but only for Pa β and Br γ lines. We computed the mean values of these two \dot{M}_{acc} estimates, plotting the results as blue filled squares. Differently, Kóspál et al. (2018) and Tofflemire et al. (2017) provided \dot{M}_{acc} of the DQ Tau source from photometry data, using an empirical relation between the luminosity excess in the U -band and the accretion luminosity (Gullbring et al. 1998). Black solid and grey dashed lines are histograms from Kóspál et al. (2018) and Tofflemire et al. (2017), respectively, where the peaks correspond to the mean value for the same phase of several periods. Fig. 9 shows that the trend with respect the phase between the samples is the same, so \dot{M}_{acc} is larger nearby the periastron in every sample, but results obtained from photometry are about a factor of two smaller than \dot{M}_{acc} computed from emission lines. This difference can be explained by both the different method used, and the fact that histograms show average values of tens of orbits, while our results and results by Muzerolle et al. (2019) are computed in a specific phase. The \dot{M}_{acc} in the four samples were computed by using different techniques, different data at different wavelengths, in different orbits. Moreover, all the methods are based on empirical relations which, therefore, are both affected by large uncertainties. Considering all these differences, it is actually a significant result that the trend shown in this figure is the same for each sample, strengthening the pulsed accretion theory for the DQ Tau system.

4.7. Accretion in Binary Systems

An important aspect of accretion in close, eccentric binary systems as DQ Tau is the absence of single circumstellar disks, and the presence of a CBD around the two stars, from which the material flows to one or both components. To test this scenario, we compared line observed accretion variability in DQ Tau with results from theoretical simulations of binary systems provided by Günther & Kley (2002a). Fig. 10 shows the mean values of the \dot{M}_{acc} for four sources. Two of them, GG Tau and UY Aur, are wide systems with little eccentricity ($e = 0.25$ and $e = 0.16$, respectively), while DQ Tau and AK Sco are close eccentric binaries ($e = 0.556$ and $e = 0.469$, respectively). The authors conclude that the only reason why \dot{M}_{acc} of wide binaries is comparable with \dot{M}_{acc} of close binaries is that the disk mass (M_{disk}) for GG Tau and UY Aur is three orders of magnitude larger, suggesting that the closer are the two components, the more efficient is the accretion process. We scaled the results of DQ Tau to the distance adopted in this work, for a coherent comparison. Fig. 10 shows that results by Günther & Kley (2002a) are in agreement with the ones we computed nearby the periastron. And our estimate for the less accreting epoch, is in agreement within the error with measurements by Gullbring et al. (1998). This suggests that Günther & Kley (2002a) simulations nicely reproduced the measured mass accretion rate for DQ Tau at periastron, but somehow overestimated the accretion during other orbital phases.

4.8. Accretion from single stars in the DQ Tau system

The main goal of this work is to determine whether both the components of DQ Tau are accreting during each epoch we observed and, if so, which one is accreting the most. For this purpose, we need two conditions to be satisfied: *i*) the two components are spectroscopically resolved; *ii*) the accretion luminosity is not too faint, so, the lines which trace accretion are detected. With these general rules in mind, we studied the accretion tracer lines for all the epochs in Fig. 11 (and in Figs. 15, 16, 17, 18, and 19 in Appendix B), similarly to what was done by Tofflemire et al. (2019) for TWA 3A system.

We identified which source is accreting the most by studying the velocity of the two peaks. We interpret that the primary (secondary) is accreting the most when the highest peak velocity corresponds to the RV of the primary (secondary). Fig. 12 shows this result by putting red for primary and blue for secondary filled circle symbols. When the two peaks, corresponding to the two RVs, are equal, then both components likely accrete at equal rates (purple filled circle). All the other cases, when it is not possible to provide information on ac-

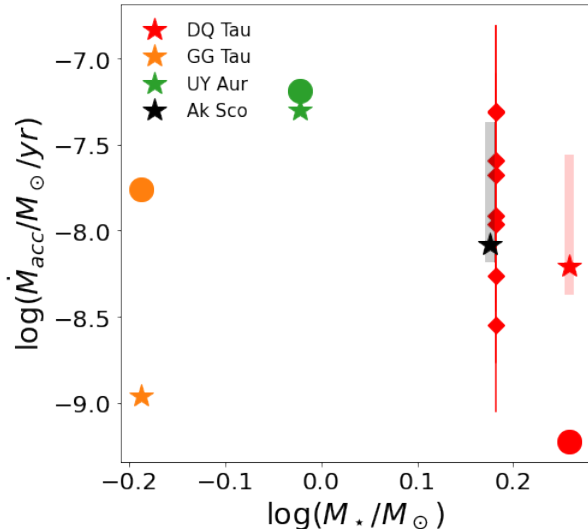


Figure 10. Mass accretion rate versus stellar mass. Günther & Kley (2002b) simulation results (mean values) for four eccentric binary systems and relative measurement by Gullbring et al. (1998) are plotted as stars and circles, respectively. Vertical red and black regions correspond to the accretion variability range obtained from simulations in five different orbits. The colors and names of the systems are reported in the legend. DQ Tau mass accretion rates of this work are marked with red diamonds.

cretion on single sources from these lines, are marked with a cross. Thus, according to Fig. 12, the primary is accreting the most during Epoch 1, at $\phi = 0.9$, and the secondary is accreting the most during Epoch 7, at $\phi = 0.98$. For all other epochs, the main accretor changes depending on which accretion tracer line is considered.

A plausible interpretation of this change in the main accretor is that different lines are formed in different regions of the accretion column. It has been shown that Balmer series lines are thought to be emitted by the pre-shock gas, in the outermost part of the inner disk. On the contrary, Paschen lines are mostly emitted in the post-shock gas (Alcalá et al. 2014; Hartmann et al. 2016, and references therein). Thus, the H I lines we see at the same epoch are tracing the flow which is reaching the shock region (Balmer series, Fig. 15) or the gas that has already been shocked (Paschen series, Fig. 17). In other words, Paschen lines show the accretion material in a region closer to the stellar surface while the material traced by the Balmer lines is still farther away from the stellar surface. Thus, looking at the same epoch but at different lines in Fig. 11, we see emission from the accreting flows in different regions. Because the main accretor changes with the orbital phase, sometimes we see “new” material (Balmer series) which is going to accrete a cer-

tain component, while “old” material (Paschen series) is accreting on the other component.

In general, narrow components (NCs) are usually formed in the post-shock region, close to the stellar surface, while broad components (BCs) in the pre-shock region (Hartmann et al. 2016). We should also remember that actual accretion flows are not homogeneous in density or temperature, so they could be explained as a superposition of accretion columns (Hartmann et al. 2016). This means that, in principle, different elements with different density and temperature develop different accretion columns. This may explain why using different lines gives different accretion rates. Averaging the different values provides the mean value of the accretion flow in the overall inner disk. Focusing only on a certain line provides a different estimate, tracing accretion from a specific region, under specific physical conditions.

In our analysis, we prefer to analyze narrow lines because they are spectroscopically resolved and formed closer to the stellar surface. In that sense, they provide a better estimate of the amount of material that is going to fall on a certain component. For our purpose, it is also important that the line is not blue or redshifted. According to the literature (Hartmann et al. 2016, and references therein), H α and [O I] lines are usually blueshifted by wind and/or jets, while H β , Pa γ , Na I doublet are usually redshifted with respect the velocity of the star, by the magnetospheric infall. Some lines might also be both blue and redshifted, this is the case of He I at 1083.0 nm. Therefore, these lines are not suitable for our purpose. On the contrary, He I at 587.65 nm and Ca II triplet emission lines have usually a very narrow component and are centered at the stellar velocity, likely tracing the post-shocked region, making these lines perfect for our study. Unfortunately, as shown in Fig. 11, the He I at $\lambda = 587.65$ nm line presents two peaks only in one epoch. For this reason, we decided that for the epochs in which the main accretor changes by looking at different lines: we established which component accretes the most by examining the Ca II triplet. For Epoch 4, where Ca II is not detected, we assumed that the secondary is the main accretor because we see differently only at H α . The H α line is generally strong and broad, and being sensitive to the blue shifting due to the optically thick regime (Hartmann et al. 2016), is not reliable for this kind of analysis.

Based on these arguments and looking at Fig. 12, we can conclude there is a periodic trend: before the periastron ($\phi = 0.98$) the secondary is accreting the most, then, right after the periastron ($\phi = 0.04$, Epoch 8), the primary is the main accretor and in the post-shocked region, according to the Paschen series, the accretion is

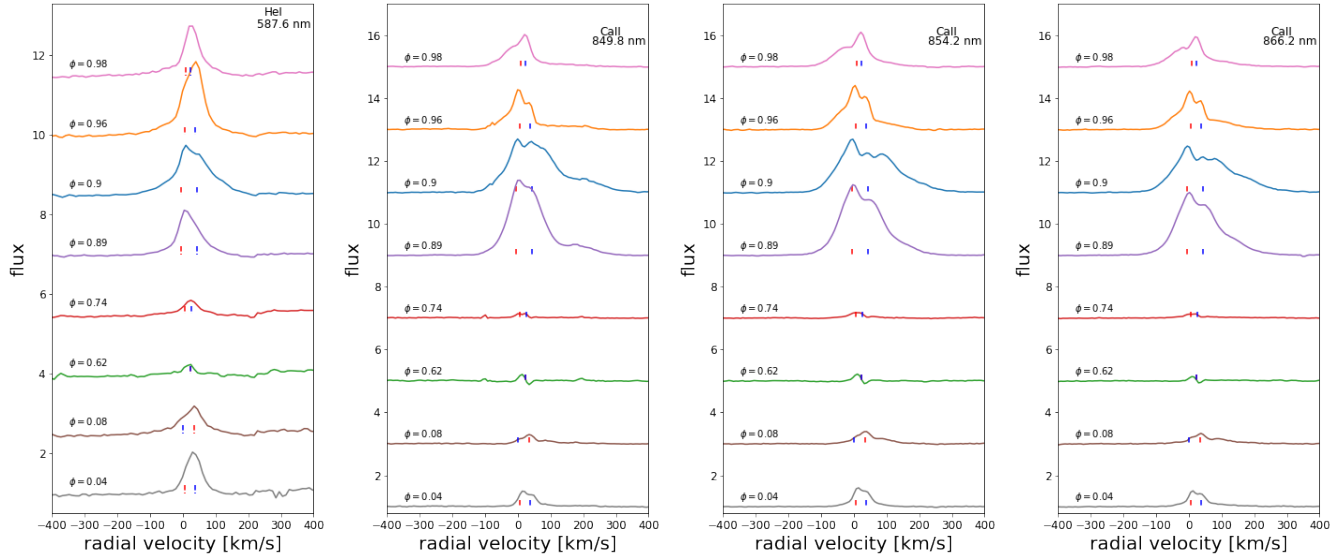


Figure 11. Velocity structure of continuum-normalized He I at $\lambda = 587.65$ nm and Ca II triplet emission lines observed by X-Shooter. Vertical red and blue dashed lines are velocities of the primary and secondary component, respectively. Spectra are ordered from bottom to top by increasing orbital phase, which is labeled adjacent to each spectrum. The line color marks the epoch, using the same colors of Fig. 6.

equally distributed between the two components, suggesting that in the future the main accretor will change. Indeed, the primary is still the main accretor at $\phi = 0.08$ (Epoch 6), even if, looking at Pa β and Pa γ the secondary is already accreting the most. Unfortunately, at $\phi = 0.62$ (Epoch 3), the two components have the same RV, so we are not able to evaluate accretion on single stars for this epoch. Later, at $\phi = 0.74$ (Epoch 4), the secondary is accreting the most. Then the accretion flows change again, directed toward the primary at $\phi = 0.89$ and 0.90 , which are Epochs 5 and 1, respectively. Finally, at $\phi = 0.96$ (Epoch 2), the secondary is still the main accretor, while some lines predict the primary is going to be the component which will accrete the most, as it is indeed at Epoch 7 ($\phi = 0.98$). We note that the change in the main accretor is not related to the absolute value of the mass accretion rate.

We would like to stress that what we know about the region where a line is produced is based on single stars, whose accretion is driven by a strong magnetic field whose main component is a dipole, and the disk we refer to is the circumstellar disk. DQ Tau is a binary system that can be treated as a single star, with the circumbinary disk acting as the circumstellar disk in a single star, nearby periastron, when the magnetic field of the two components merges in a dipole magnetic field (Salter et al. 2010). This is all we can say based on the emission lines. Further insights may be gained from studying the magnetic fields that ultimately determines the path of accretion in the magnetospheric accretion model. Mapping the magnetic field of stars is possible, e.g., us-

ing spectropolarimetric methods, and such a study for DQ Tau is in progress using CFHT/ESPaDONs spectra (Pouilly et al., in prep.).

The fact that the main accreting component changes is, in principle, not in agreement with numerical simulations that predict that the secondary should always be the dominant accretor in a binary system (e.g. Hayasaki et al. 2007, 2013; Farris et al. 2014b; Young & Clarke 2015). These predictions are based on the fact that the angular momentum for the two sources should be the same, and as the secondary is less massive, it is located farther from the center of mass of the system. In other words, the secondary is closer to the CBD, where it should be easier to trap the accreting flow. But, for DQ Tau, because the two components have very similar masses, it is not surprising that the main accretor can change epoch by epoch, and this still satisfy the theoretical basis of the numerical simulations. However, the change in the main accreting component is predicted by both Günther & Kley (2002a) and Muñoz & Lai (2016), although the timescales for which such switch of the main accretor is considered is about 100 orbital period, while we see the change in the main accretor component three times in less than two orbital periods.

5. SUMMARY AND CONCLUSIONS

We studied the accretion variability of the young eccentric binary system DQ Tau, by analyzing 8 epochs of X-Shooter spectra taken over 7 orbital periods. We estimated the RVs, the veiling, the spectral type, the extinction and the disk mass of DQ Tau system. We

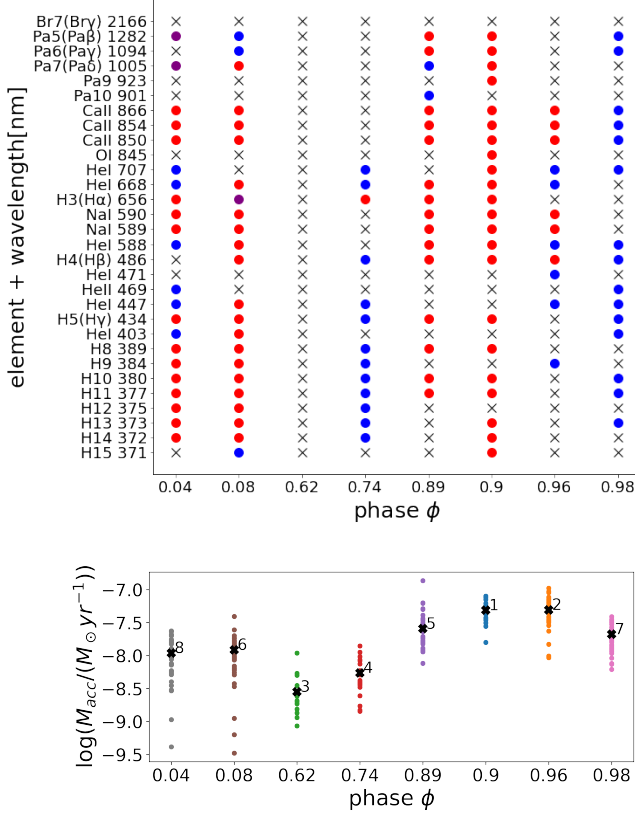


Figure 12. *Top:* Filled circles shows whether the highest peak of the line corresponding to the element in y-axis in a certain epoch, has the radial velocity of the primary (red) or the secondary (blue) component, or there are two peaks of the same intensity corresponding to both the RVs (purple). Black crosses highlight line profiles for which is not possible to determine which source is accreting the most either because there is no detection, or because the two components are not spectroscopically resolved. *Bottom:* Co-added mass accretion rate of the two components as a function of the orbital phase, as in Fig. 6.

subtracted the chromospheric and the photospheric contributions from the observed spectra, to isolate the accretion component. We studied the accretion process of DQ Tau system comparing it with single stars, previous literature about DQ Tau, and other binary systems. We were able to select the main accretor epoch by epoch, and discuss its variability. Our main conclusions are:

- DQ Tau is a binary system composed of two early-M type stars (M0), with extinction of $A_V = 1.72 \pm 0.26$ mag, in agreement with the previous literature.

- We measured RVs, resolving the RVs of the two DQ Tau components for seven epochs. Our results are in agreement with the Keplerian solutions by Czekala et al. (2016).
- The veiling changes with orbital phase, time, and wavelength, in a similar way to accretion variability, confirming its correlation with the mass accretion rate.
- Our results on \dot{M}_{acc} variability with the phase confirm the pulsed accretion model, showing larger mass accretion rate nearby periastron and are in agreement with previous results of DQ Tau mass accretion rate computed using different techniques.
- The accretion luminosity and the mass accretion rate of DQ Tau are compatible with L_{acc} and \dot{M}_{acc} of 2-3 Myr old CTTs, following the same relations with respect to the stellar parameters, if we consider the contribution of the two components.
- The main accretor in DQ Tau system varies epoch by epoch. This contradicts those simulations that predict that the secondary is always the main accretor in eccentric binary systems. Other simulations predict that the main accretor should change, but on significantly longer time scales than what we observe here.

ACKNOWLEDGMENTS

This project has received funding from the European Research Council (ERC) under the European Union’s Horizon 2020 research and innovation programme under grant agreement No 716155 (SACCRED).

This work is based on observations collected at the European Southern Observatory under ESO programme 090.D-0446 by Salter & Kafka We thank Dr. Stella Kafka for kindly providing us the X-Shooter date used in this work.

We thank the anonymous referee for their effort in reviewing this paper, which help us to improve it.

Facilities: ESO-VLT/XSHOOTER

Software: molecfit (Smette et al. 2015; Kausch et al. 2015b); SAPHIRES <https://github.com/tofflemire/saphires>; barycorrpy (Kanodia & Wright 2018).

A. FLUX CALIBRATION

In order to check the quality of our flux calibration, we compared the photometry we used (observed or inferred depending on the epoch) with the synthetic photometry obtained by convolving the spectrum with the filter bandpasses, band by band. Figure 13 shows the general agreement within the observed/inferred and the synthetic photometry, for each epoch.

B. ALL THE ACCRETION LINES

We present in this section all the lines profile that trace accretion in DQ Tau. Results are summarized in the text, in Fig. 12.

REFERENCES

- Alcalá, J. M., Manara, C. F., France, K., et al. 2019, *A&A*, 629, A108, doi: [10.1051/0004-6361/201935657](https://doi.org/10.1051/0004-6361/201935657)
- Alcalá, J. M., Natta, A., Manara, C. F., et al. 2014, *A&A*, 561, A2, doi: [10.1051/0004-6361/201322254](https://doi.org/10.1051/0004-6361/201322254)
- Alcalá, J. M., Manara, C. F., Natta, A., et al. 2017, *A&A*, 600, A20, doi: [10.1051/0004-6361/201629929](https://doi.org/10.1051/0004-6361/201629929)
- Alcalá, J. M., Gangi, M., Biazzo, K., et al. 2021, *A&A*, 652, A72, doi: [10.1051/0004-6361/202140918](https://doi.org/10.1051/0004-6361/202140918)
- Andrews, S. M., Wilner, D. J., Espaillat, C., et al. 2011, *ApJ*, 732, 42, doi: [10.1088/0004-637X/732/1/42](https://doi.org/10.1088/0004-637X/732/1/42)
- Antoniucci, S., Giannini, T., Li Causi, G., & Lorenzetti, D. 2014, *ApJ*, 782, 51, doi: [10.1088/0004-637X/782/1/51](https://doi.org/10.1088/0004-637X/782/1/51)
- Artymowicz, P., & Lubow, S. H. 1994, *ApJ*, 421, 651, doi: [10.1086/173679](https://doi.org/10.1086/173679)
- . 1996, *ApJL*, 467, L77, doi: [10.1086/310200](https://doi.org/10.1086/310200)
- Bailer-Jones, C. A. L., Rybizki, J., Fouesneau, M., Demleitner, M., & Andrae, R. 2021, *AJ*, 161, 147, doi: [10.3847/1538-3881/abd806](https://doi.org/10.3847/1538-3881/abd806)
- Basri, G., & Batalha, C. 1990, *ApJ*, 363, 654, doi: [10.1086/169374](https://doi.org/10.1086/169374)
- Cardelli, J. A., Clayton, G. C., & Mathis, J. S. 1989, *ApJ*, 345, 245, doi: [10.1086/167900](https://doi.org/10.1086/167900)
- Coelho, P., Barbuy, B., Meléndez, J., Schiavon, R. P., & Castilho, B. V. 2005, *A&A*, 443, 735, doi: [10.1051/0004-6361:20053511](https://doi.org/10.1051/0004-6361:20053511)
- Czekala, I., Andrews, S. M., Torres, G., et al. 2016, *ApJ*, 818, 156, doi: [10.3847/0004-637X/818/2/156](https://doi.org/10.3847/0004-637X/818/2/156)
- Dodin, A. V., & Lamzin, S. A. 2012, *Astronomy Letters*, 38, 649, doi: [10.1134/S1063773712100027](https://doi.org/10.1134/S1063773712100027)
- D’Orazio, D. J., Haiman, Z., & MacFadyen, A. 2013, *MNRAS*, 436, 2997, doi: [10.1093/mnras/stt1787](https://doi.org/10.1093/mnras/stt1787)
- Erlick, C., Frederick, J. E., Saxena, V. K., & Wenny, B. N. 1998, *J. Geophys. Res.*, 103, 31,541, doi: [10.1029/1998JD200053](https://doi.org/10.1029/1998JD200053)
- Farris, B. D., Duffell, P., MacFadyen, A. I., & Haiman, Z. 2014a, *ApJ*, 783, 134, doi: [10.1088/0004-637X/783/2/134](https://doi.org/10.1088/0004-637X/783/2/134)
- . 2014b, *ApJ*, 783, 134, doi: [10.1088/0004-637X/783/2/134](https://doi.org/10.1088/0004-637X/783/2/134)
- Fiorellino, E., Manara, C. F., Nisini, B., et al. 2021, *A&A*, 650, A43, doi: [10.1051/0004-6361/202039264](https://doi.org/10.1051/0004-6361/202039264)
- Folha, D. F. M., & Emerson, J. P. 1999, *A&A*, 352, 517
- Gullbring, E., Hartmann, L., Briceño, C., & Calvet, N. 1998, *ApJ*, 492, 323, doi: [10.1086/305032](https://doi.org/10.1086/305032)
- Günther, R., & Kley, W. 2002a, *A&A*, 387, 550, doi: [10.1051/0004-6361:20020407](https://doi.org/10.1051/0004-6361:20020407)
- . 2002b, *A&A*, 387, 550, doi: [10.1051/0004-6361:20020407](https://doi.org/10.1051/0004-6361:20020407)
- Hartigan, P., Edwards, S., & Ghandour, L. 1995, *ApJ*, 452, 736, doi: [10.1086/176344](https://doi.org/10.1086/176344)
- Hartmann, L., Calvet, N., Gullbring, E., & D’Alessio, P. 1998, *ApJ*, 495, 385, doi: [10.1086/305277](https://doi.org/10.1086/305277)
- Hartmann, L., Herczeg, G., & Calvet, N. 2016, *ARA&A*, 54, 135, doi: [10.1146/annurev-astro-081915-023347](https://doi.org/10.1146/annurev-astro-081915-023347)
- Hayasaki, K., Mineshige, S., & Sudou, H. 2007, *PASJ*, 59, 427, doi: [10.1093/pasj/59.2.427](https://doi.org/10.1093/pasj/59.2.427)
- Hayasaki, K., Saito, H., & Mineshige, S. 2013, *PASJ*, 65, 86, doi: [10.1093/pasj/65.4.86](https://doi.org/10.1093/pasj/65.4.86)
- Herbig, G. H. 1977, *ApJ*, 214, 747, doi: [10.1086/155304](https://doi.org/10.1086/155304)
- Herczeg, G. J., & Hillenbrand, L. A. 2014, *ApJ*, 786, 97, doi: [10.1088/0004-637X/786/2/97](https://doi.org/10.1088/0004-637X/786/2/97)
- Kanodia, S., & Wright, J. 2018, *Research Notes of the American Astronomical Society*, 2, 4, doi: [10.3847/2515-5172/aaa4b7](https://doi.org/10.3847/2515-5172/aaa4b7)
- Kausch, W., Noll, S., Smette, A., et al. 2015a, *A&A*, 576, A78, doi: [10.1051/0004-6361/201423909](https://doi.org/10.1051/0004-6361/201423909)
- . 2015b, *A&A*, 576, A78, doi: [10.1051/0004-6361/201423909](https://doi.org/10.1051/0004-6361/201423909)
- Kochanek, C. S., Shappee, B. J., Stanek, K. Z., et al. 2017, *PASP*, 129, 104502, doi: [10.1088/1538-3873/aa80d9](https://doi.org/10.1088/1538-3873/aa80d9)
- Koornneef, J. 1983, *A&A*, 500, 247
- Kóspál, Á., Ábrahám, P., Zsidi, G., et al. 2018, *ApJ*, 862, 44, doi: [10.3847/1538-4357/aacafa](https://doi.org/10.3847/1538-4357/aacafa)
- Kurosawa, R., & Romanova, M. M. 2013, *MNRAS*, 431, 2673, doi: [10.1093/mnras/stt365](https://doi.org/10.1093/mnras/stt365)
- Kurosawa, R., Romanova, M. M., & Harries, T. J. 2008, *MNRAS*, 385, 1931, doi: [10.1111/j.1365-2966.2008.13055.x](https://doi.org/10.1111/j.1365-2966.2008.13055.x)

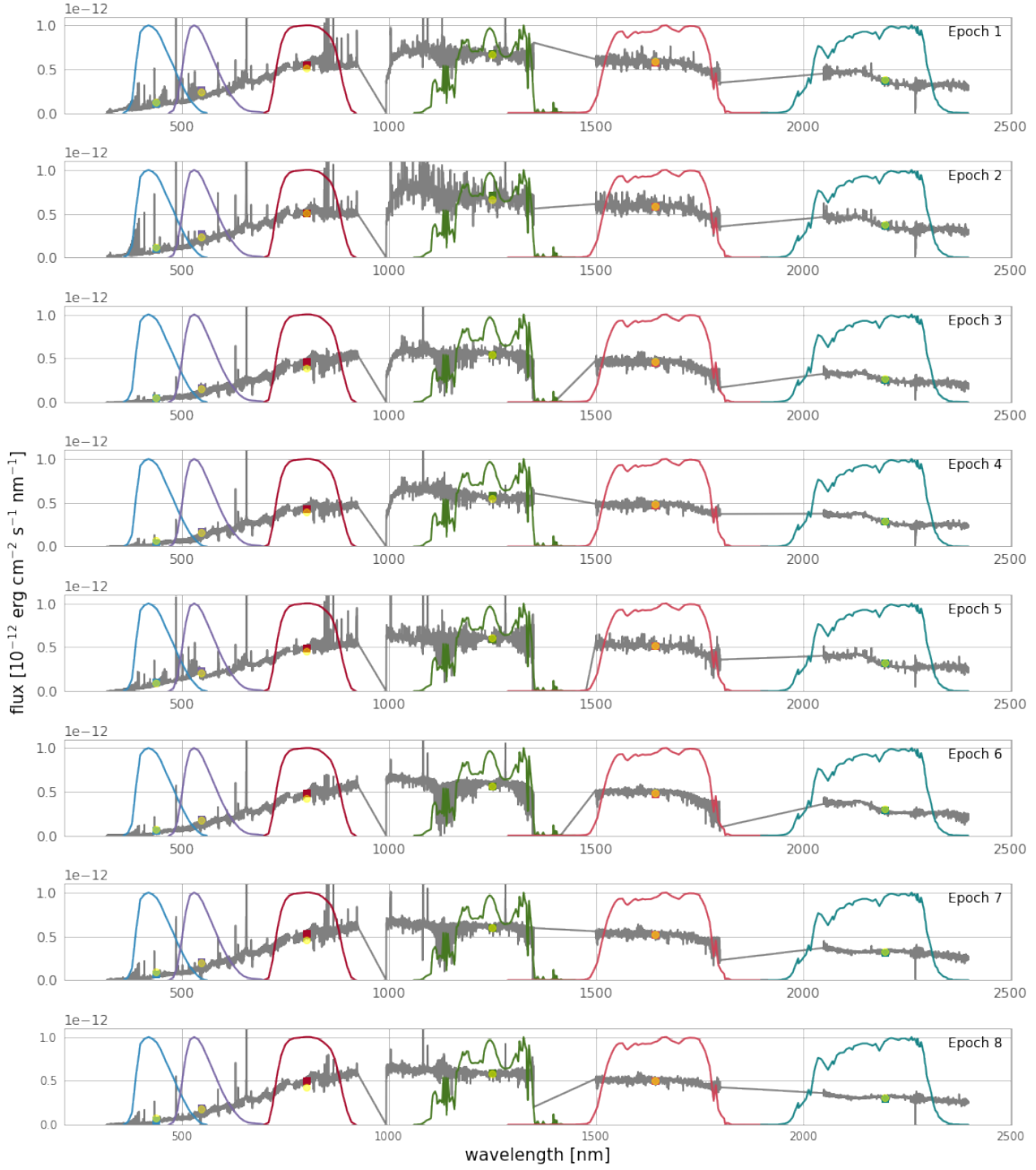


Figure 13. X-Shooter flux-calibrated spectrum from Epoch 1 (top) to Epoch 8 (bottom) are shown in grey. Yellow circles represent the observed or inferred photometry at each band. The filter bandpasses (lines) and the synthetic photometry (filled squares) obtained integrating the spectrum over these bandpasses are overlaid.

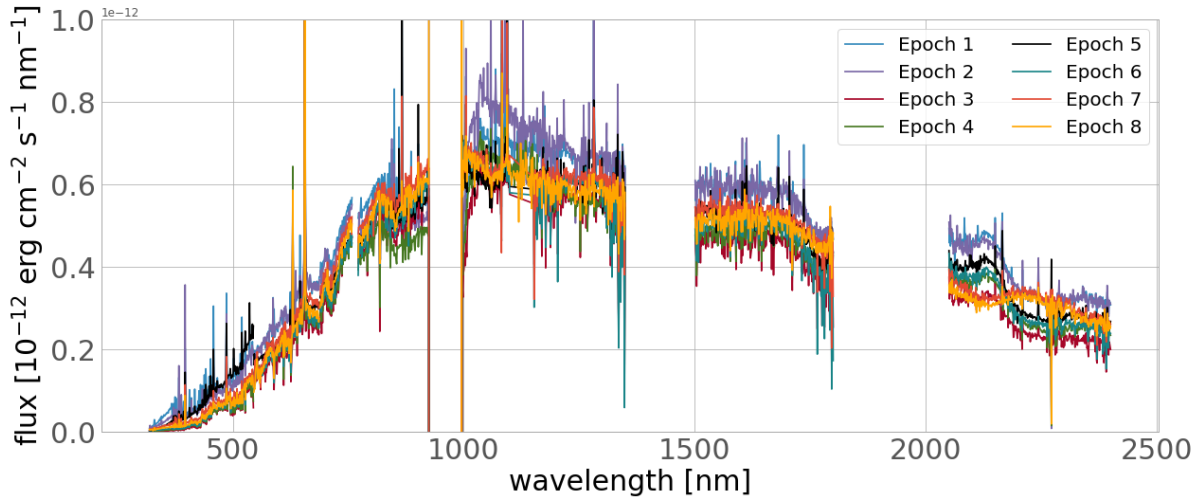


Figure 14. DQ Tau smoothed and flux calibrated spectra.

- Manara, C. F., Mordasini, C., Testi, L., et al. 2019, *A&A*, 631, L2, doi: [10.1051/0004-6361/201936488](https://doi.org/10.1051/0004-6361/201936488)
- Manara, C. F., Testi, L., Rigliaco, E., et al. 2013, *A&A*, 551, A107, doi: [10.1051/0004-6361/201220921](https://doi.org/10.1051/0004-6361/201220921)
- Manara, C. F., Testi, L., Herczeg, G. J., et al. 2017, *A&A*, 604, A127, doi: [10.1051/0004-6361/201630147](https://doi.org/10.1051/0004-6361/201630147)
- Mathieu, R. D., Stassun, K., Basri, G., et al. 1997, *AJ*, 113, 1841, doi: [10.1086/118395](https://doi.org/10.1086/118395)
- Meyer, M. R., Calvet, N., & Hillenbrand, L. A. 1997, *AJ*, 114, 288, doi: [10.1086/118474](https://doi.org/10.1086/118474)
- Monin, J. L., Clarke, C. J., Prato, L., & McCabe, C. 2007, in *Protostars and Planets V*, ed. B. Reipurth, D. Jewitt, & K. Keil, 395
- Muñoz, D. J., & Lai, D. 2016, *ApJ*, 827, 43, doi: [10.3847/0004-637X/827/1/43](https://doi.org/10.3847/0004-637X/827/1/43)
- Muzerolle, J., Flaherty, K., Balog, Z., Beck, T., & Gutermuth, R. 2019, *ApJ*, 877, 29, doi: [10.3847/1538-4357/ab1756](https://doi.org/10.3847/1538-4357/ab1756)
- Muzerolle, J., Hartmann, L., & Calvet, N. 1998, *AJ*, 116, 455, doi: [10.1086/300428](https://doi.org/10.1086/300428)
- Newnham, D. A., & Ballard, J. 1998, *J. Geophys. Res.*, 103, 28,801, doi: [10.1029/98JD02799](https://doi.org/10.1029/98JD02799)
- Rei, A. C. S., Petrov, P. P., & Gameiro, J. F. 2018, *A&A*, 610, A40, doi: [10.1051/0004-6361/201731444](https://doi.org/10.1051/0004-6361/201731444)
- Rigliaco, E., Natta, A., Testi, L., et al. 2012, *A&A*, 548, A56, doi: [10.1051/0004-6361/201219832](https://doi.org/10.1051/0004-6361/201219832)
- Romanova, M. M., & Owocki, S. P. 2016, *Accretion, Outflows, and Winds of Magnetized Stars*, Vol. 54, 347
- Salter, D. M., Kóspál, Á., Getman, K. V., et al. 2010, *A&A*, 521, A32, doi: [10.1051/0004-6361/201015197](https://doi.org/10.1051/0004-6361/201015197)
- Shappee, B. J., Prieto, J. L., Grupe, D., et al. 2014, *ApJ*, 788, 48, doi: [10.1088/0004-637X/788/1/48](https://doi.org/10.1088/0004-637X/788/1/48)
- Smette, A., Sana, H., Noll, S., et al. 2015, *A&A*, 576, A77, doi: [10.1051/0004-6361/201423932](https://doi.org/10.1051/0004-6361/201423932)
- Tofflemire, B. M., Mathieu, R. D., Ardila, D. R., et al. 2017, *ApJ*, 835, 8, doi: [10.3847/1538-4357/835/1/8](https://doi.org/10.3847/1538-4357/835/1/8)
- Tofflemire, B. M., Mathieu, R. D., & Johns-Krull, C. M. 2019, *AJ*, 158, 245, doi: [10.3847/1538-3881/ab4f7d](https://doi.org/10.3847/1538-3881/ab4f7d)
- Vernet, J., Dekker, H., D’Odorico, S., et al. 2011, *A&A*, 536, A105, doi: [10.1051/0004-6361/201117752](https://doi.org/10.1051/0004-6361/201117752)
- Young, M. D., & Clarke, C. J. 2015, *MNRAS*, 452, 3085, doi: [10.1093/mnras/stv1512](https://doi.org/10.1093/mnras/stv1512)

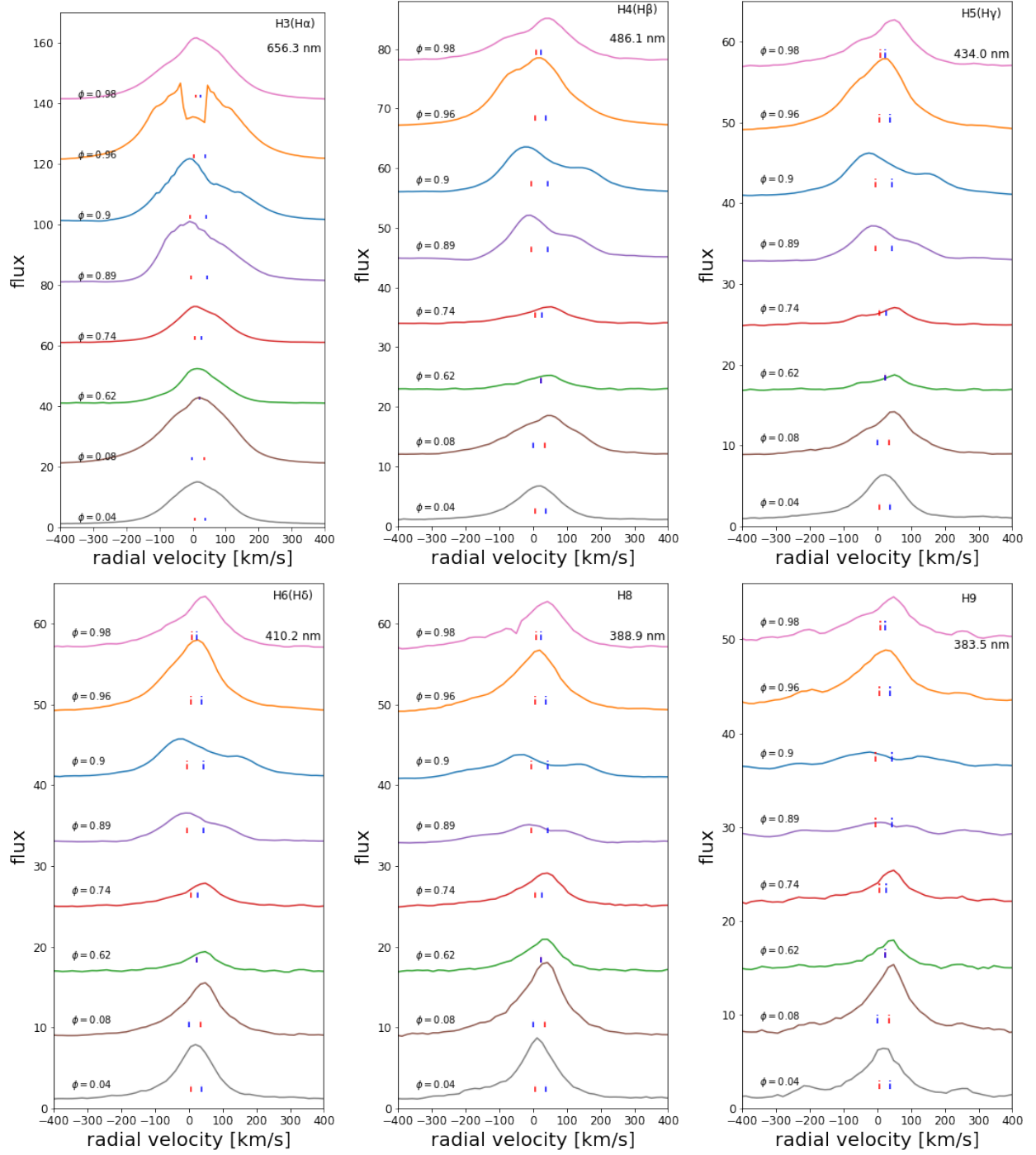


Figure 15. Velocity structure of continuum-normalized H I emission lines as indicated in the figures, observed by X-Shooter in UVB and VIS. Vertical red and blue dashed lines are velocities of the two primary and secondary component, respectively. Spectra are ordered from bottom to top by increasing orbital phase, which is labeled adjacent to each spectrum. The line color marks the epoch, using the same colors of Fig. 6.

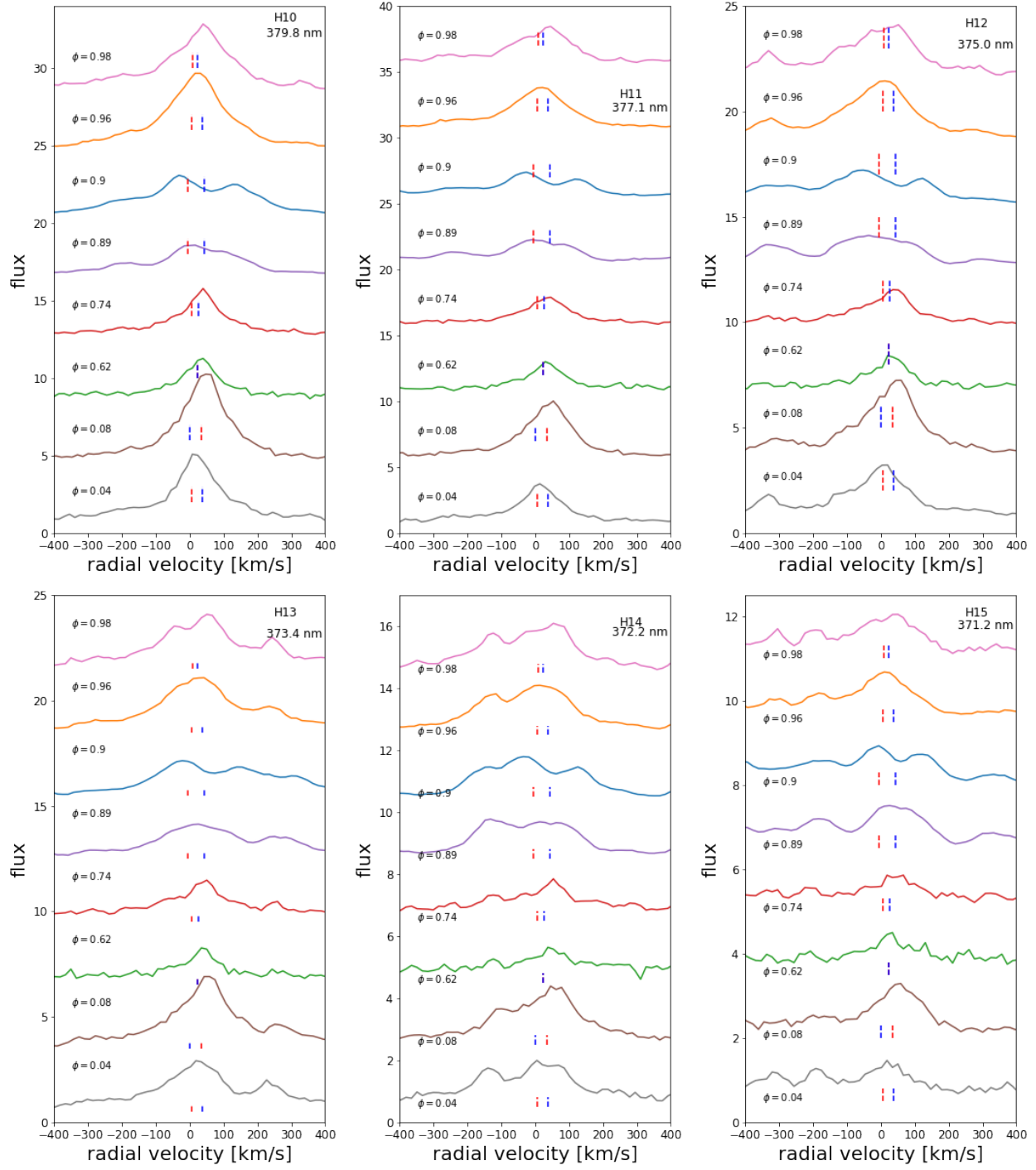


Figure 16. Velocity structure of continuum-normalized HI emission lines as indicated in the figures, observed by X-Shooter in UVB and VIS. Vertical red and blue dashed lines are velocities of the primary and secondary component, respectively. Spectra are ordered from bottom to top by increasing orbital phase, which is labeled adjacent to each spectrum. The line color marks the epoch, using the same colors of Fig. 6.

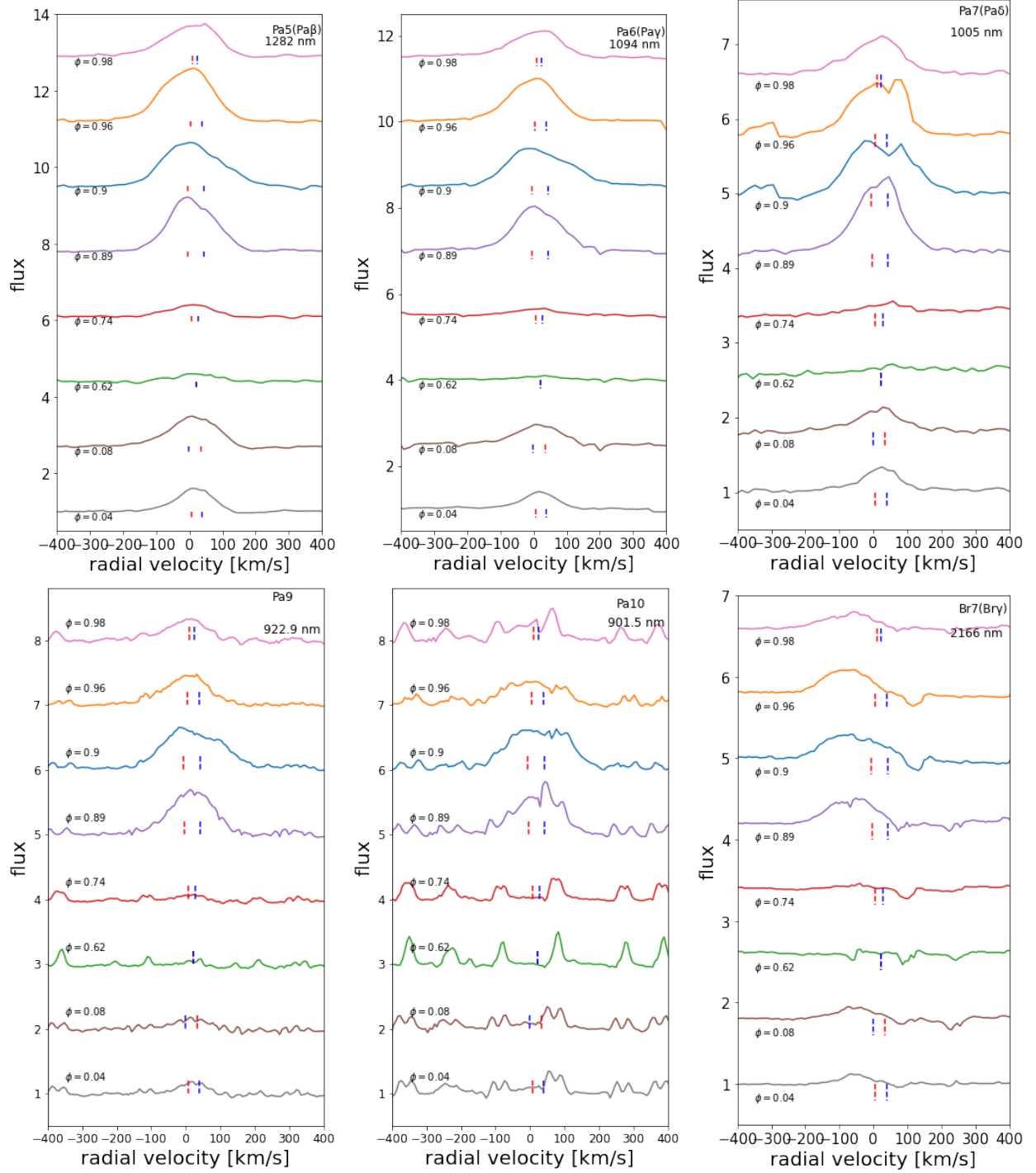


Figure 17. Velocity structure of continuum-normalized H I emission lines as indicated in the figures, observed by X-Shooter in NIR. Vertical red and blue dashed lines are velocities of the primary and secondary component, respectively. Spectra are ordered from bottom to top by increasing orbital phase, which is labeled adjacent to each spectrum. The line color marks the epoch, using the same colors of Fig. 6.

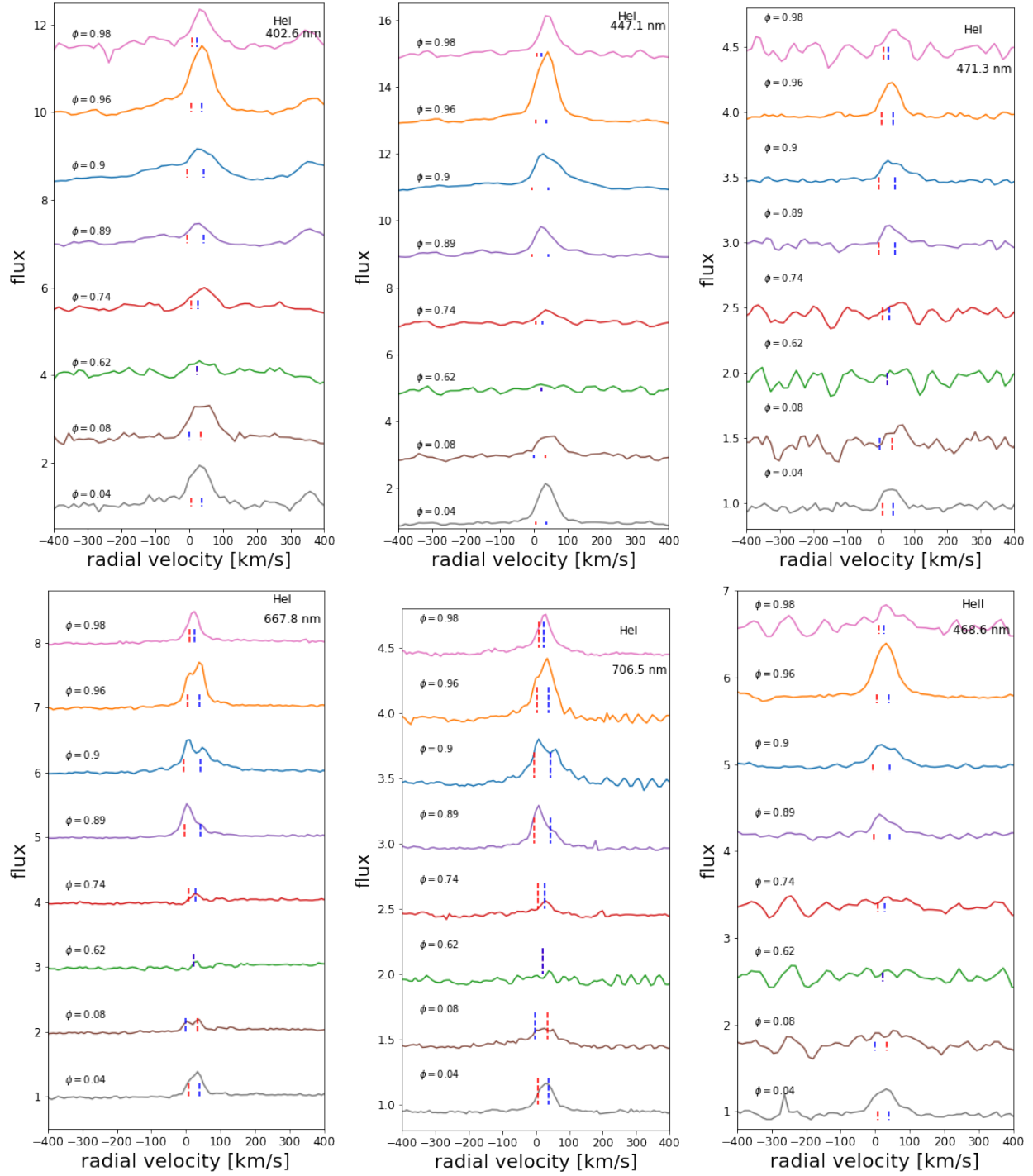


Figure 18. Velocity structure of continuum-normalized HeI and HeII emission lines as indicated in the figures, observed by X-Shooter. Vertical red and blue dashed lines are velocities of the primary and secondary component, respectively. Spectra are ordered from bottom to top by increasing orbital phase, which is labeled adjacent to each spectrum. The line color marks the epoch, using the same colors of Fig. 6.

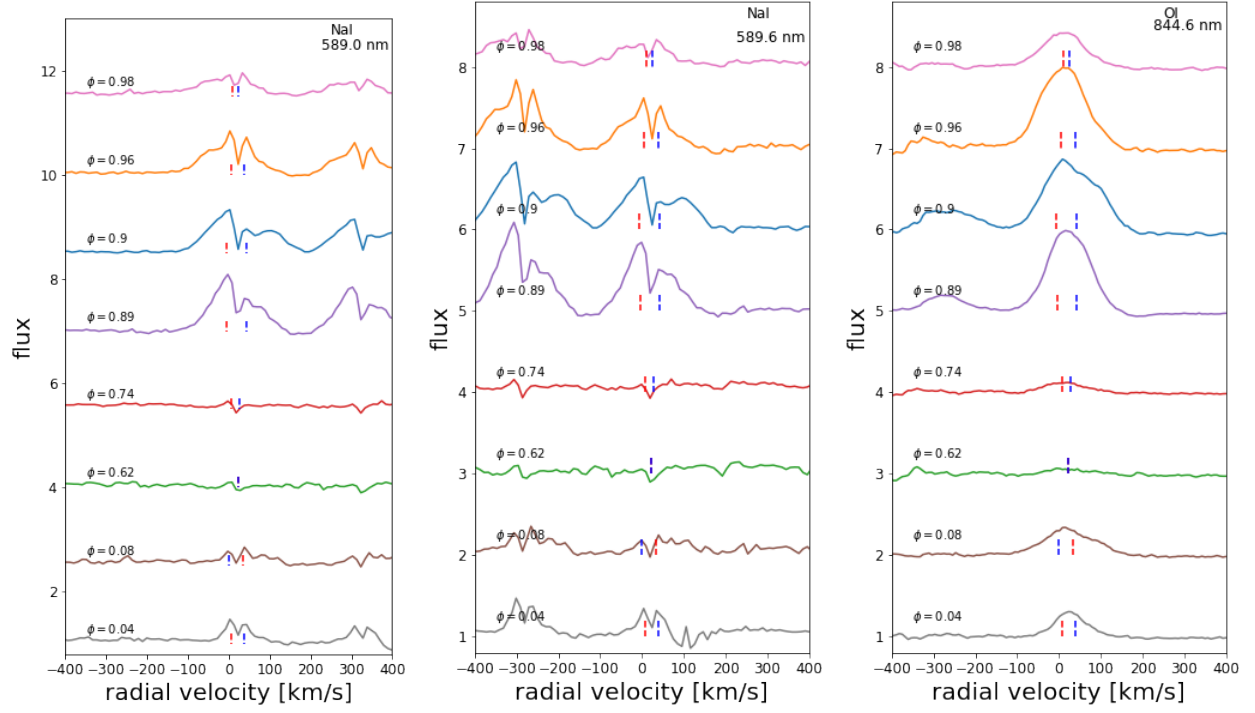


Figure 19. Velocity structure of continuum-normalized CaII triplet, NaI doublet, and OI emission lines as indicated in the figures, observed by X-Shooter. Vertical red and blue dashed lines are velocities of the primary and secondary component, respectively. Spectra are ordered from bottom to top by increasing orbital phase, which is labeled adjacent to each spectrum. The line color marks the epoch, using the same colors of Fig. 6.